University of Zurich[UZH]

Zurich Open Repository and Archive
University of Zurich
University Library
Strickhofstrasse 39
CH-8057 Zurich
www.zora.uzh.ch

Year: 2011

Resolving the baryon-fraction profile in lensing galaxies

Leier, D ; Ferreras, I ; Saha, P ; Falco, E E

DOI: https://doi.org/10.1088/0004-637X/740/2/97

Posted at the Zurich Open Repository and Archive, University of Zurich
ZORA URL: https://doi.org/10.5167/uzh-54742
Journal Article
Accepted Version

Originally published at:
Leier, D; Ferreras, I; Saha, P; Falco, E E (2011). Resolving the baryon-fraction profile in lensing galaxies. Astrophysical Journal, 740(2):97.
DOI: https://doi.org/10.1088/0004-637X/740/2/97

Accepted for publication in the Astrophysical Journal
Preprint typeset using LaTeX style emulateapj v. 11/10/09

arXiv:1102.3433v2 [astro-ph.GA] 28 Jul 2011

RESOLVING THE BARYON-FRACTION PROFILE IN LENSING GALAXIES

Dominik Leier[1], Ignacio Ferreras[2], Prasenjit Saha[3], and Emilio E. Falco[4]

Draft version July 29, 2011

ABSTRACT

The study of the distribution of baryonic matter within dark halos enriches our understanding of galaxy formation. We show the radial dependence of stellar baryon fraction curves derived for 21 lensing galaxies from the CfA-Arizona Space Telescope LEns Survey by means of stellar population synthesis and pixel-based mass reconstruction. The sample covers a stellar mass range of $M_s \simeq 2\times10^9 - 3\times10^{11} M_\odot$ (solar masses) which corresponds to a total enclosed mass range of $M_L \simeq 7\times10^9 - 3\times10^{12} M_\odot$ on radial scales from $0.25R_e$ to $5R_e$ (effective radii). By examining the M_s and M_L dependence on radial distance to the centre of each galaxy we find that there are pairs of lenses on small to intermediate mass scales which approach at large radii the same values for their enclosed total mass but exhibit very different stellar masses and stellar baryon fractions. This peculiar behaviour subsides for the most massive lensing galaxies. All the baryon fraction profiles show that the dark matter halo overtakes the stellar content between 1.5 and $2.5R_e$. At $3R_e$ most of the stellar component is enclosed. We find evidence for a stellar baryon fraction steadily declining over the full mass range. Furthermore, we shed light on the Fundamental Plane puzzle by showing that the slope of the $M_L(<R)$-to-$M_s(<R)$ relation approaches the mass-to-light relation of recent Fundamental Plane studies at large radii. We also introduce novel concentration indices $c = R90/R50$ for stellar and total mass profiles (i.e., the ratio of radii enclosing 90% and 50% of the stellar or total mass). We show that the value $c = 2.6$ originally determined by light profiles which separates early-type galaxies from late-type galaxies also holds for stellar mass. In particular, less massive dark matter halos turn out to be influenced by the distribution of stellar matter on resolved scales below 10 kpc. The ongoing study of resolved baryon fraction profiles will make it possible to evaluate the validity of star formation models as well as adiabatic contraction prescriptions commonly used in simulations.

Subject headings: gravitational lensing - galaxies: elliptical and lenticular, cD - galaxies: evolution - galaxies: halos - galaxies: stellar content - dark matter.

1. INTRODUCTION

The physics driving the evolution from the collapse of gas and dark matter halos to the formation of galaxies remains one of the open questions in astrophysics. In general, star formation efficiency — viewed as the stellar to total mass fraction within the virial radius of a halo — is highest for galaxies similar to the Milky Way, with an efficiency decreasing towards higher and lower masses (Moster et al. 2010). The lower escape velocities in less massive galaxies allow the gas to be ejected by stellar feedback (Larson 1974; Dekel & Silk 1986). Supernova-induced winds are energetic enough to significantly impede galaxy formation at baryonic masses below $10^{11}M_\odot$ (Brooks et al. 2007). Such feedback regulates the star formation efficiency, which is responsible for the mass-metallicity relation (Tremonti et al. 2004). For more massive galaxies, an Active Galactic Nucleus (AGN) is believed to account for the decreasing efficiency (see e.g. Di Matteo et al. 2005). This feedback mechanism explains the exponential cut-off in the luminosity function, either by the thermal coupling of AGN outflows with gas (e.g. Tabor & Binney 1993; Croton et al. 2006; Bower et al. 2006) or by mechanical feedback that prevents gas cooling (Sijacki et al. 2007).

Observational estimates of the stellar baryon fraction are thus an essential piece of the puzzle and provide important constraints on simulations, especially at the sub-grid level that describes the baryon physics of galaxy formation. They also help to understand the nature of the scaling relations, such as the Fundamental Plane and its projections. Currently, most of the studies that resolve the central regions of galaxies on scales below 10 kpc are based on dynamical models applied to the kinematics of stars (see e.g. Cappellari et al. 2006; Coccato et al. 2009). Similarly, lensing studies on galaxy scales are usually based on a parametric decomposition of the stellar and dark matter component (see e.g. Auger et al. 2010; Trott et al. 2010), with its inherent degeneracies. Over larger scales, Guo et al. (2010) and Moster et al. (2010) match the stellar mass function of SDSS galaxies with the distribution of dark matter halos from numerical simulations to find stellar baryon fractions $f_b \sim 3-4\%$ — significantly lower than the cosmological fraction $f_b = \Omega_b/\Omega_m = 0.17$ (Dunkley et al. 2009) — with a maximum for galaxies with halo masses around $10^{12}M_\odot$. However, this approach is only valid for masses enclosed within the virial radius, and cannot resolve the radial dependence, which offers valuable information about how baryons build galaxies. For instance, the velocity dispersion analysis

[1] Astronomisches Rechen-Institut, Zentrum für Astronomie, Universität Heidelberg, Mönchhofstr. 12-14, D-69120 Heidelberg, Germany; leier@ari.uni-heidelberg.de
[2] Mullard Space Science Laboratory, University College London, Holmbury St Mary, Dorking, Surrey RH5 6NT, UK
[3] Institute for Theoretical Physics, University of Zürich, Winterthurerstrasse 190, CH-8057 Zürich, Switzerland
[4] Harvard-Smithsonian Center for Astrophysics, 60 Garden Street,Cambridge, MA 02138, USA

of Lintott et al. (2006) on a sample of SDSS early-type galaxies gives within the effective radius a low baryon fraction ($f_b \sim 8\%$) which is lower than the cosmological value, but twice as large as determined within the virial radius, illustrating the importance of a resolved estimate of the baryon fraction within galaxy halos. Galaxy formation models combining the evolution of the dark matter and gaseous components along with a set of sub-grid prescriptions for star formation and feedback (see e.g. Kauffmann et al. 1993; Cole et al. 1994; Croton et al. 2006) are only indirect methods with considerable uncertainties. Indeed, robust observational estimates of the baryon fraction on galaxy scales are needed to properly constrain the recipes included in these models.

Gravitational lensing opens a door to smaller scales over which baryonic processes are important. For instance, one can explore concentrations and baryon fractions giving good evidence of adiabatic contraction, as done e.g. by Jiang & Kochanek (2007). They analyze the relation between stellar baryon fraction and concentration in adiabatic and non-adiabatic models. Mandelbaum et al. (2006) present a galaxy-galaxy weak lensing analysis of a large sample of early and late-type galaxies. They obtain stellar surface masses depending on radius with a resolution down to 10 kpc. However, their approach is also based on a halo-model to describe the relation of galaxies and dark matter.

The use of mass models and model-based prescriptions introduces hard-to-quantify deviations from real mass distributions, especially over the scales of a few R_e that we want to investigate. Assuming a mass model for a lensing system excludes mass distributions which are not accessible in the parameter-space of the model and introduces the problem of model non-uniqueness. To avoid this, free-form methods are necessary. In this paper, we use the *PixeLens* method of (Saha & Williams 2004; Coles 2008) to reconstruct the surface mass density of a sample of lens galaxies. For the stellar component — which represents the vast majority of the baryons in the inner regions of early-type galaxies — the photometric data is used to constrain a large volume of stellar population synthesis (SPS) models (Ferreras et al. 2005, 2008). The combination of both lensing and stellar mass in a pixel-based manner allows for a two-dimensional mapping of the baryon fraction. Choosing a sample of moderate redshift lenses enables us to determine the lensing profile out to a few R_e. The CASTLES sample[5] fulfills this requirement. We present in this paper an analysis of the enclosed stellar and total mass content in a sample of 21 lensing galaxies out to a radial distance of $\sim 1.5 - 2$ times the Einstein radius, i.e. up to several R_e.

In section 2 we discuss briefly the lens sample with respect to environment, lens morphology and photometric properties. By means of three lens systems, arguably rather extreme, we illustrate the subtleties of photometric modeling and the authenticity of lenses. The latter point refers to unlensed double quasars which mimic a lens system with a doubly imaged quasar. We will show how a real lens can be distinguished from a spurious system in our analysis. We test the reliablility of our photometry-based results by comparing inferred stellar surface mass densities with equivalent results from Ferreras et al. (2009) and Shen et al. (2003).

Section 4 presents the results of this study regarding the radial dependence of enclosed stellar versus total lens mass. We continue in section 5 with a closer examination of the stellar and total mass concentration and define a simple model to study the energetic evolution of early type galaxies. The conclusion and discussion section 6 summarizes our findings and puts them into the context of recent work on galaxy formation.

2. SAMPLE PROPERTIES

In the following we compare lens samples in general with respect to their environment. We also explain how the environment affects the lens systems and continue with a detailed one-by-one study of the lenses used in this analysis according to their photometric and morphological properties. To get a clear view on lens galaxies whose baryonic content we want to determine, we need to correct the data for light originating from the quasar images, by means of PSF subtraction and masking.

The selection criteria for our lens sample are as follows. For the lens mass reconstruction we must have the redshifts of the source and the lens as well as accurate image positions. The stellar population synthesis analysis demands a sufficient separation between lens and quasar images in order to extract uncontaminated photometric estimates from the lens. Furthermore, NIR imaging must be available.

Constraining the SPS models using photometry in several bands is desirable, although we note that our reference H-band is the F160W filter of HST/NICMOS. For the redshift of most of the lenses, this band maps a rest-frame region that does not change significantly for the colours found in these galaxies. We discuss in this section the available multiband data and respective PSFs used for the modeling of the surface brightness distribution. Finally we discuss outliers and special cases for comparison. All information regarding lens galaxy properties, their environment and photometry is given in Table 1 and Table 2.

2.1. *The Environment*

To describe a lens with respect to its environment, one has to keep in mind that the lens shear required by (parametric and non-parametric) lens models can be due to physically interacting galaxies or to line-of-sight objects. Regarding the former, one could estimate how the environment of the lens galaxy evolved in its recent past, whereas any line-of-sight objects are naturally unrelated to the local region of the lens. Nevertheless these two sources for shear are hard to distinguish. If located in a group or cluster environment, X-ray measurements are expected to give reliable constraints on the DM content (Buote & Tsai 1995) and thus a hint about the direction and strength of the shear. Only a few lens environments have been studied so far for CASTLES lenses (e.g. Fassnacht et al. 2006; Momcheva et al. 2006).

[5] http://www.cfa.harvard.edu/castles

The environment for a sample of 70 SLACS lenses has been studied by Treu et al. (2009); they find $17 \pm 5\%$ are in overdense regions. For our sample of 21 CASTLES lenses we find that 7 galaxies are located in groups and 3 in clusters. Four galaxies have one close galaxy or possible companion with which they may interact gravitationally. For the remaining 7, no large shear contribution is required and no close galaxies have been found. Thus we find that $\sim 50\%$ of our galaxies lie in overdense regions. The lower fraction found by Treu et al. (2009) is likely due to the smaller redshift range of SLACS (up to $z \approx 0.5$) and the property of the SDSS selection function to pick lenses whose Einstein radius is about the fibre-radius of the SDSS spectrograph (3 arcsec).

2.2. *The Sample*

In the following we briefly discuss the lens sample. In addition to the previous paragraph we provide information about the environment which in fact influences both the mass model and the light profile and yields important insights into the evolution of early-type galaxies. After giving the full name of the lenses we use their abbreviations only. The method used to model the lenses is explained in detail in section 3.3. Figure 15 shows the appearance of the free-form mass models.

For 9 lensing systems all three bands were used to constrain a large number of SPS models, which consequently sets constraints on the colour-to-mass relation. Another 8 lenses could be analysed in H and I band. The remaining 4 lenses had suitable data in H band only.

First, we describe the 9 lenses with suitable data in all three wavebands.

The four-image lens system ("quad") **B0712+472** is one of the few lenses for which a *TinyTim* PSF was sufficient to remove quasar images in H band. In V and I band the quasar images could all be masked out. Lens models found in previous studies require significant external shear, which can be attributed to 9 or more galaxies in a foreground group at $z \sim 0.3$ found by Fassnacht & Lubin (2002). Their study also shows one other galaxy at the redshift of B0712 at $\sim 100''$ from the lens.

The quads **B1422+231**, **B2045+265**, **Q0047-2808**, **Q2237+030** undergo the following treatment. In both I and V bands, *TinyTim* provided a suitable PSF. In the H band an isolated star taken from the same or a contemporaneous NICMOS image was used for convolution and point-source fitting if needed. B1422 is in a poor group with 5 nearby galaxies mostly south east of the lens that cause a significant shear (Momcheva et al. 2006; Hogg & Blandford 1994). The group is visible in X-rays at $0.5 - 2$ keV (Momcheva et al. 2006). In recent work by Wong et al. (2011) 12 new members were found to be part of the group. B2045 as found by Fassnacht et al. (1999) might be influenced by a group of galaxies west of the lens. A shear in this direction is also required by the lens model. The lens might also be affected by a close dwarf galaxy causing anomalous flux ratios (McKean et al. 2007). Q0047 is a lens with only a small shear required by lens models. However, Wong et al. (2011) find evidence for a galaxy group with 9 members. In the case of the Einstein Cross Q2237 the bulge of a spiral galaxy is responsible for the lensing. The system shows only a mild external shear due to the disk of the spiral galaxy.

For spiral galaxies the contribution of dust to the photometry is usually more significant than for early-type galaxies (the latter morphological type constitute the majority of our lensing galaxies). However, we note that in the case of Q2237, the redshift of the lens is very low, which implies that our reference photometric band (H) maps a similar wavelength range in the *rest frame*, where dust attenuation is less severe. From the estimates of Eigenbrod et al. (2008) on VLT/FORS1 spectra of Q2237, we infer a contribution from dust in the H band photometry of Q2237 at the level of 0.05 mag (Ferreras et al. 2010).

For lenses **BRI0952-0115**, **Q0142-100** and **PG1115+080** extensive use of the iteration method described in section 3.1 was made if the quasar images could not be masked out. The environments of the doubly imaged quasars BRI0952 and Q0142 have been studied by Lehár et al. (2000), Momcheva et al. (2006) and Eigenbrod et al. (2007) and found to have no dominant impact on the total shear beyond a cosmological (large-scale structure) contribution $\gamma_{\rm LSS}$ which is additionally confirmed by lens models. BRI0952 was previously thought to reside in a region loosely bound to a poor group with 5 members (Momcheva et al. 2006); a later study found it is at higher redshift and thus not connected with the group (Eigenbrod et al. 2007). For Q0142 there is not much known about the close-in group environment, although there are some galaxies near the line-of-sight, whose redshifts are mostly unknown. Surdej et al. (1987) speculate that a galaxy about $10''$ away from the lens may be a group member. The environment of the quad PG1115 is thoroughly analyzed by Momcheva et al. (2006). They find 13 galaxies in a local group with elongated group emission in X-rays according to Grant et al. (2004). The brightest 4 members of the group are located on an axis with a position angle of $+60°$ (measured North through East) of the lens mass which accounts well for the shear required in our lens model.

The two-image lens **HS0818+1227** requires special treatment as we use an isolated PSF of image B1030+071 to fit the quasar image in the H band. In the I and V bands, the quasar images are used for fitting. Iteration as it is used for enhancing PSFs of other lenses does not provide better model fits for the lens because of the large separation between images and lens. The image separation is $2.56''$. Hence the reduction process is further simplified by masking. Since its discovery by Hagen & Reimers (2000) no further insights into the environmental properties of the lens are available. Nevertheless Hagen & Reimers (2000) found a galaxy $5''$ north of the lens which appears to have the same redshift of $z = 0.39$, which explains the external shear required by our lens model. A chain of galaxies at a distance of $10''$ north-east could also be associated with the lens galaxy.

Next, we describe the 8 lenses with suitable data in two wavebands.

For the quad **B1608+656** and the doubles **HE1104-1805** and **HE2149-2745** H and I band data could be

used to isolate the lens galaxy. According to More et al. (2009) **MG2016+112** exhibits quadruply imaged features of the quasar jet which can be distinguished only in the radio band. We take account of the rather complex structure in the lensing part of our analysis. For all their H band images, a sufficiently isolated star with fitted background extracted from the image of MG0414+0534 was used to remove the quasar images with an acceptable goodness of fit.

B1608 resides in the middle of a galaxy group with 8 other group members according to Fassnacht et al. (2006). The photometry shows an object close to the main galaxy, which constitutes a second lens galaxy. This is confirmed by the reconstructed mass map (Fig. 15) as it predicts a conspicuously elongated mass distribution towards NE. Images also show a prominent dust lane between the two galaxies. However, we analyzed the impact of dust reddening on our results, as shown in Appendix B for B1608 and B1600. The uncertainty due to dust on $\log(M_s)$ is in both cases not larger than 0.3 dex.

MG2016 is known to be a giant elliptical galaxy in a cluster with 69 probable photometrically selected members of many different galaxy types (Toft et al. 2003). Among them is a significant fraction of merging cluster galaxies, which is direct evidence for a hierarchical formation history (van Dokkum et al. 2000). Most of the neighbouring objects within $30''$ lie on an east-west axis and thus explain the major shear direction. HE1104 features the second highest image separation of $3.19''$ and a distinct lens galaxy (the median separation is $\sim 1.5''$). Furthermore the lens appears to be near the bright image which is rather unusual and implies the presence of a group or cluster enhancing the separation (Lehár et al. 2000). Parametric as well as free-form mass models also suggest that an external shear is mandatory to reproduce the image configuration (e.g. Wisotzki et al. 1998). The lens galaxy is unaffected by quasar light allowing for a good fit. However, the photometric redshifts of a few neighbouring galaxies described in Faure et al. (2004) indicate that such cluster galaxies are probable companions of the lensed quasar rather than of the lens. The double HE2149 might be a member of a cluster as inferred by Lopez et al. (1998) by a large number of red nonstellar objects in R-band images of the field around the lens. Considering recent estimates of the lens redshift from Eigenbrod et al. (2007) ($z_{\rm lens} = 0.603$) and the environment survey from Momcheva et al. (2006) HE2149 could be in a group with 3 neighbouring objects. The morphology of the lens shows no sign of strong external shear.

The doubly imaged quasar **SBS1520+530** is treated like the previous doubles but with a star from the same image file in preference to other PSFs. This lens is a member of a galaxy group with at least 4 other members as stated in Auger et al. (2008).

For the two quads **MG0414+0534**, **RXJ0911+0551** and the double **Q0957+561** we obtain good residual maps by means of the iteration method. MG0414 at $z = 0.960$ is the second most distant lens of our sample. Judging by its luminosity and colour, the lens is likely to be a passively evolving early-type galaxy (Tonry & Kochanek 1999). Schechter & Moore (1993) find an object close to image B visible only in I-band, which might contribute to the lensing effect. Our reconstructed mass map also shows increased surface density at the position of the object. RXJ0911 is located on the outskirts of a cluster (Morgan et al. 2001). *Chandra* observations of the cluster suggest a complex non-spherical cluster mass distribution at a temperature of roughly 2.3 keV. Q0957, found by Walsh et al. (1979), is special in several ways. First there is a doubly imaged galaxy component in addition to the famous double quasar used to calculate the projected mass map. Secondly the lens is a cD galaxy located in the centre of a cluster. The nearest cluster member lies within $10''$ East of the lens galaxy. However a simple external shear is insufficient to describe the effect of the environment on the image positions. Breaking the degeneracy between the shape of the galaxy and the cluster shear takes advantage of arc features (Keeton et al. 2000) and X-ray data as attempted by Chartas et al. (1998).

Finally, we describe all the lenses with suitable data in only one waveband.

B1030+071, **B1152+200** and **B1600+434** are treated similarly with regard to the fitting routine, i.e. the isolated outermost quasar image was used for subtraction and convolution. The three doubles have comparable angular image separations and average velocity dispersions as well as intermediate luminosities. Observed substructures in B1030 indicate the presence of an interacting galaxy system (Jackson et al. 2000) although firm statements about the environment cannot be made (Lehár et al. 2000). However, shear is not strongly required by our mass model. For B1152 there is no information about the composition of the environment. Judging by the morphology of the image-source system no strong shear is expected. B1600 is located in a denser group with at least 6 late-type galaxies (Auger et al. 2007) which cause significant shear. The absence of X-ray emission is suggestive of a not relaxed group, a conclusion strengthened by the elongated morphology of the group. Furthermore the lens galaxy appears to be almost edge-on and exhibits a prominent dust lane. As remarked above, dust reddening changes the population synthesis input and leads to underestimated stellar content, but even for the extreme cases in our sample the effect of dust on inferred stellar masses cannot be larger than 0.3 dex (see Appendix B).

For the doubly imaged quasar **LBQS1009-0252** the star in the H-band image of MG0414 is used again as a PSF with sufficient quality for the fit. Lehár et al. (2000) locate the lens galaxy close to quasar image B. They find that a dominant shear contribution of the host galaxy of a n earby quasar ($4.6''$ northwest of the lens — unrelated to the lensed quasar) is consistent with the derived major axis of the lens when modeled by a Singular Isothermal Ellipsoid. Using a singular isothermal sphere model Claeskens et al. (2001) determine a smaller shear. Faure et al. (2004) state that there is no significant galaxy overdensity in the field. This is in agreement with the free-form lens models of this study, which do not require external shear for this lens.

2.3. *Outliers And Special Cases*

We now briefly describe three special cases, **B0218+357**, **B1933+503** and **RXJ0921+4529**.

With the first two we want to demonstrate the impact properties like small image separations and interfering luminous structures can have on the goodness of the SPS. The third lens shows how spurious lenses, i.e. galaxies with nearby quasars which are not lensed images of the same background object, behave in this analysis. All three lenses are excluded from our analysis.

For B0218 as for 10 other systems in our sample a star was used to fit the quasar images in the H-band. Since B0218 is the system with the smallest image separation ($0.33''$) known, it is extremely difficult to separate the lens galaxy from the images of the background quasar. The system is an extreme case in several aspects and a good example for showing the impact of degeneracies between the magnitudes of overlapping objects. B0218 unlike any other lens in the sample did not yield reasonable Sersic profile parameters as the wings of the quasar PSFs overlap with the lens. For an unconstrained fit the combined light from the quasar images and lens galaxy results most likely in an overestimated magnitude of the PSFs. However after attempting to fit the lens system only by PSFs, a Sersic profile is needed to achieve an acceptable residual map. Even though one cannot obtain zero residuals by fitting only two point sources, there are several combinations of Sersic profile magnitudes and two PSF magnitudes that result in the same total surface brightness profile. Bearing this in mind, we use the fitting parameters with the best χ^2, which also yields an acceptable residual map, to carry out the SPS. The projected lens mass map shows that external potentials induce a shear in B0218 that was studied in Lehár et al. (2000). They find 13 possibly perturbing galaxies inside a radius of $20''$ located roughly along the axis which connects the two quasar images. It should be mentioned that B0218 is according to Lehár et al. (2000) a late-type galaxy which causes the SPS to predict a different mass content.

B1933, discovered by Sykes et al. (1998), has 10 distinct images formed from a three-component source, promising an exceptionally well-constrained mass profile. A star in the same H-band image was used for convolution. There is as yet no study of the environment of the lens but according to the mass reconstruction, no strong shear is necessary to explain the morphology. The resolved features of the lensed background object cannot be fitted by PSF but are taken out of the fitting routine by using circular masks with a 5 pixel radius, a size chosen to cover features distinguishable from background and still show enough of the lens galaxy to allow for a reasonable fit. The trade-off between light contamination due to minimal masking and information loss due to aggressive masking is in any case problematic. In the case of B1933 almost the whole inner region is surrounded by masked regions causing the fit parameters R_e and n to diverge. Setting a constraint on the Sersic index ($n \leq 4$) is necessary. Despite all attempts at modeling this lens, it remained a persistent outlier, and hence is removed from the analysis.

The double RXJ0921, has the highest angular image separation ($6.93''$) compared to any other lens in the sample. According to Muñoz et al. (2001) it is probably a member of an X-ray cluster. From model fits of the host galaxy Peng et al. (2006) conclude that RXJ0921 is a binary quasar rather than a gravitational lens. Also Popović et al. (2010) find quite different spectral properties in the spectra of the two components. For now we assume the system is a lens. Since even the smaller lens-image distance is above $3''$ and the quasar images are isolated, we obtain a high-quality fit by taking the quasar image as a PSF for both overall convolution and quasar subtraction. No constraints are necessary. There are 16 objects within $20''$ from the lens galaxy. Only for three of them a redshift close to that of the lens could be determined. The mass model however does not require an external shear. In contrast to all other lenses, RXJ0921 (when treated as a lens) turns out to exhibit an unusually low stellar-mass fraction and an almost constant $M_L(< R)$ profile. The peculiar properties of RXJ0921 can be taken as further evidence against the lens hypothesis as suspected in aforementioned studies.

3. ANALYSIS TECHNIQUE

In this section we describe necessary steps to obtain baryon-fraction profiles. As explained before we need to free the lens galaxies in given multiband data from interfering light, originating from quasar images, to obtain best-fitting surface brightness profiles. This reduction step is shown in the following paragraph. The output is used to constrain SPS models and to estimate pixel-by-pixel the stellar mass via the colour-to-mass relation, as described in section 3.2. Combining stellar mass estimates and pixel-based mass reconstruction (section 3.3) yields baryon-fraction profiles for the given set of lens galaxies.

3.1. *Preparing Photometry*

The problems arising during this procedure can be assigned to one of the following categories: (a) finding an appropriate PSF for convolution and point-source reduction, or (b) removing perturbing light sources that negatively affect the fitting procedure. The latter includes masking of image regions as well as fitting of additional light profiles to structures which clearly do not belong to the lens. Since we use photometric data in different filters (V,I and H bands), one of the following PSF-picking procedures has to be suitably chosen for each band.

1. Find an isolated star from the same or a contemporaneous (as nearly as possible) image and extract it and a sufficiently large surrounding region not contaminated by light from the lens system or other sources; hereafter referred to as the *star-picking method*.

2. Select the outermost image of a lens system and use it for the quasar image fitting. While the lens galaxy and the other quasar images are fitted with GALFIT (Peng et al. 2002), the residual image, showing only the previously chosen outermost image without any contaminating light, can then be taken as a qualitatively refined PSF. This step can be repeated until we reach the desired level of enhancement. This procedure will be referred to as the *iteration* method. In some cases, when the picked quasar image was sufficiently isolated, iteration brought no further improvement.

3. Using a synthetic PSF generated by *TinyTim* (Krist 1993) yields better results for WFPC2 images rather than for NICMOS data (presumably due to the higher stability of WFPC2 PSFs).

Methods (1) to (3) were combined with *masking* of quasar images or any other luminous structure interfering with the fit. To prevent the fit from diverging, in some cases further constraints are necessary.

Details of the constraints applied to each lens can be found in Table 2. In the following, we give an overview of the types of constraints we have applied to the sample:

- fixing the sky background for the already reduced images to a value we determined with SExtractor, since estimating the background is essential to extract a meaningful profile of the lens (Häussler et al. 2007), (low signal-to-noise objects are thus neglected, increasing the goodness of the fit for the generally bright lens galaxy),
- fixing the surface brightness profiles to previously determined (x, y) positions,
- constraining $R_{\rm e}$ and/or the Sersic index n, since both parameters are degenerate, being basically inversely related, i.e. constraining $R_{\rm e}$ to a low value causes n to diverge and vice versa,
- constraining the position angle and the axis ratio to a physically appropriate range of values, and finally
- restricting the range of magnitudes of the point sources, e.g., constraining image A to be at least 0.5 magnitudes brighter than image B.

Except for the first two constraints, which are necessary for only a few lensing systems, we try to keep the number of degrees of freedom of the fit as high as possible and fix the parameters only if there is no alternative. In cases where the best-fit PA in one band was found to differ significantly from the PA in another band, it was necessary to constrain that parameter. The same applies to the axis ratio b/a. If a highly eccentric ellipse is fitted to an actual round lens galaxy due to interfering PSF wings, the parameter space must be constrained to exclude less likely b/a values. Since both the lensing galaxies and quasar images are in some cases too bright to be distinguishable in H-band, but too faint in V-band, we use the shape parameters PA or b/a from I-band as a proxy for the fits in other bands. This was done for B1422, BRI0952, HS0818 and Q2237. This approach is legitimized by the fact that different stellar populations visible in different bands do not change their relative positions and orientations considerably. All other fitting parameters apart from the boxiness, which is set to zero throughout the process are free. The boxiness as well as all other parameters are defined in Peng et al. (2002).

To minimize χ^2 and test the stability of the fit, the fitting procedure was repeated with slight changes to the initial parameters. But χ^2 is not the only criterion to assess the quality of a fit. We focus on the goodness of the fit in regions most important to our analysis, i.e. in the central region of the lens galaxy. The ratio of the fitted image and the original image yields a percentage map of the lens systems showing pixel-by-pixel the quality of the model, as illustrated in Fig. 1. We note that in some cases, better χ^2 fits were rejected in favour of the flatness of the residual in central regions $\lesssim 1R_{\rm e}$ of the lens. This occurs in particular for the few lenses for which the short distance to a lensed quasar image makes constraints mandatory.

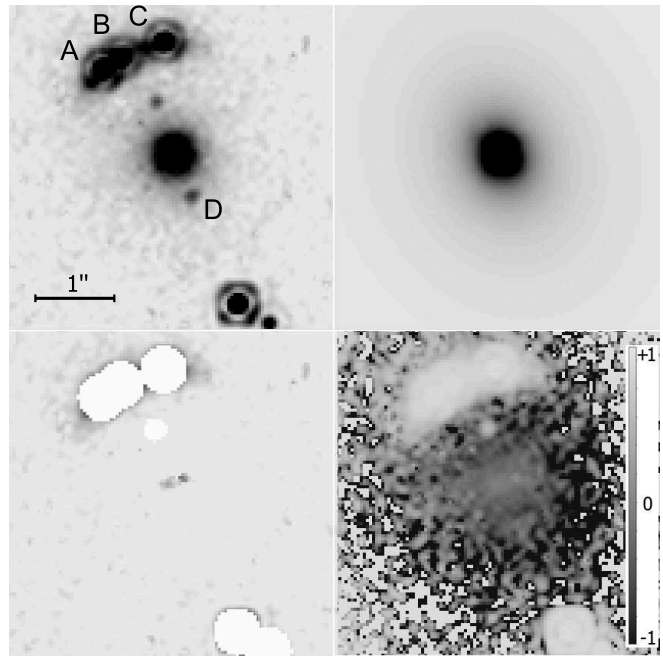

FIG. 1.— Upper left panel: original H-band NICMOS image of the lens system B2045. North is left and East is down. Best fits for the lens galaxy could be obtained by masking out images A, B, C, the stellar objects south of the lens and a "blob" West of the lens galaxy. Upper right panel: model for the lens galaxy. Lower left panel: Residual image. Lower right panel: Residual divided by original image.

For lenses with photometric data in more than one band the I or V-band parameters for $R_{\rm e}$, n, b/a and PA were taken as a prior to the H-band parameters if necessary.

3.2. *Estimating stellar masses*

Our stellar mass estimates are based on a pixel-based comparison of the best fits to the surface brightness of the lenses with stellar mass-to-light ratios (Υ) determined by population synthesis models constrained by the available photometry. Even though GALFIT does a parametric search to get the best fit, for this analysis we are just interested in the 2D distribution that minimises the residuals, regardless of the parameters themselves, i.e. we are less sensitive to the inherent degeneracies associated with parametric fits. For each lens we ran a grid of $32 \times 32 \times 32$ models, where the star formation history is described by a decaying exponential, defined by three free parameters — the quantities in parentheses denote the range explored for each one: formation epoch (defined as a redshift $2 < z_{\rm FOR} < 10$); exponential timescale ($-1 < \log(\tau/{\rm Gyr}) < 1$); and metallicity ($-1 < [{\rm m/H}] < +0.3$). Models from Bruzual & Charlot (2003) are used, assuming a Chabrier (2003) initial mass function (IMF). For each choice of the three parameters, a composite population is obtained, transformed to the redshift of the lens, and folded with the passband response of the HST V (F555W, WFPC2), I (F814W,

WFPC2) and H (F160W, NICMOS) filters to compare with the observed colours and to extract a mass-to-light ratio in the observer-frame H band. The colours are corrected for Galactic extinction using the dust maps of Schlegel et al. (1998).

We extract the stellar mass densities from the H band image (NICMOS F160W). Whenever model fits of the lens were available for I or V, the colours where used on a pixel by pixel basis to constrain Υ_H. Otherwise, we used integrated colours within an elliptical aperture defined by the half-light radius R_e of the H band image (see Table 1). In general, broadband photometry alone cannot be used to constrain the ages and metallicities of the lens galaxy. However, the stellar masses, when estimated via "red" M/L ratios, are less sensitive to the age-metallicity degeneracy (see e.g. Ferreras et al. 2008). For comparison, we provide the total stellar mass-to-light ratio in the rest-frame V-band M_s/L_V in Table 1. Colours and magnitudes are in agreement with comparable quantities in Rusin et al. (2003). The F160W band corresponds to a rest-frame wavelength between 0.8 and 1.2μm (except for Q2237, which roughly samples rest-frame H-band). Hence, for the sample considered here, the mass-to-light ratios are not affected by the presence of young stars, an issue that becomes important when dealing with optical or NUV indicators (see e.g. Rogers et al. 2010). From the modeling of the old stellar populations that these systems feature (except for lens Q2237 — which is a bulge — the other lenses are early-type galaxies), an uncertainty of $\Delta\Upsilon \lesssim 0.15$ dex is expected (Gallazzi & Bell 2009). Dust reddening, as we explain in Appendix B, leads to underestimated stellar mass. However, since no starburst galaxy is among our lenses we can safely assume that the effect of dust on M_s does not exceed 20%. The number of lenses which exhibit dusty features (e.g. B1600) is, nevertheless, small. The most significant systematic error relates to the choice of the Initial Mass Function, especially the low-mass end, which does not contribute to the light, but can contribute very significantly to the total mass content. However, frequently used choices of the IMF such as Miller & Scalo (1979), Scalo (1986), Kroupa et al. (1993) or Chabrier (2003) have similar distributions at the low mass end. It is only the traditional single-power law of the Salpeter (1955) IMF that gives different stellar mass predictions. Previous detailed work on the kinematics of nearby early-type galaxies (Cappellari et al. 2006) or strong lenses (Ferreras et al. 2008, 2010) shows that the low-mass end of the Salpeter IMF is ruled out as it predicts stellar mass surface densities higher than the dynamical or lensing estimates. However, even using a Salpeter IMF does not strongly affect our results, as they mainly focus on the scaling of the regions where dark matter dominates. Ferreras et al. (2010) illustrate differences between five different population synthesis models based on different prescriptions and/or stellar libraries. The predicted stellar masses – measured in the H band – agree to within 10%, (at fixed IMF) especially given the ages of these lenses.

To compare our lensing (early-type) galaxies with a typical field sample, we show in Fig. 2 the equivalent to the Kormendy relation (this time defined with respect to the surface stellar mass density at $1R_e$). We show as open dots the sample of ACS/GOODS early-type galaxies from (Ferreras et al. 2009), and our lensing galaxies as squares with error bars. One can see that 14 out of 18 lensing galaxies are located inside a 1σ-band around the best fit of the GOODS sample. We also provide the SDSS relation from Shen et al. (2003) as a local ($z \sim 0.1$) reference. The obvious preference of the lens sample to be at larger effective radius and smaller surface mass density is due to a selection bias, which is a combination of the lensing bias and additional requirements, such as a sufficient distinguishability from surrounding quasar images.

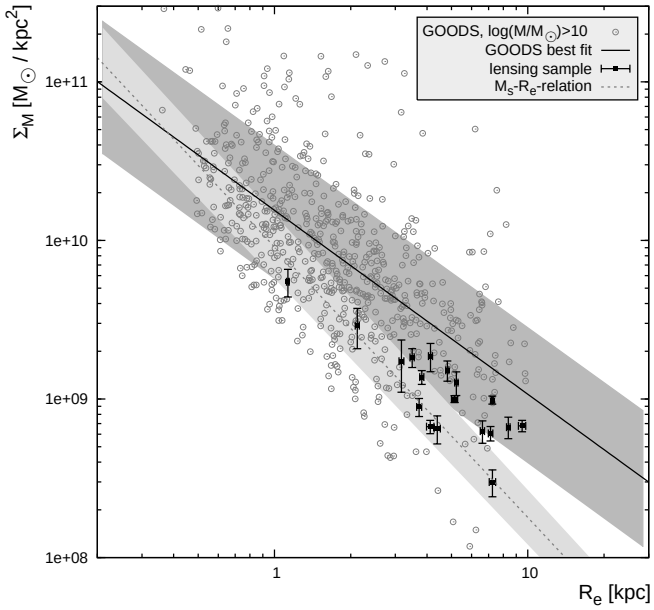

FIG. 2.— Stellar Surface Mass density at a radius of $1R_e$ versus effective radius. Early-type galaxies with stellar mass above $10^{10} M_\odot$ (open circles) selected from the Hubble Space Telescope/Advanced Camera for Surveys images of the Great Observatories Origins Deep Survey (GOODS) are shown together with our lens sample (filled squares). The dashed line denotes the stellar mass to size relation from SDSS which accounts for early-type galaxies at $z \sim 0.1$ (Shen et al. 2003).

Furthermore, as we show later in this paper, the slope of the Fundamental Plane relation $M^\eta \sim L$ can be recovered from our data. Thus we consider the lens sample representative for early-type galaxies in general.

3.3. *Reconstructing the total-mass profiles*

For each lens, the projected total-mass distribution is reconstructed on a circular field made up of 750 square tiles or pixels, each pixel consisting of a uniform non-negative mass distribution with a mass density of a few times the critical density. We provide mass reconstruction maps of the sample in Fig. 15. The pixellated mass distribution must reproduce the observations, in the following ways.

1. Multiple-image systems with the observed positions must arise as solutions of the lens equation. The images are considered to be unresolved; for extended images, the peak of their surface brightness distribution is located and considered as an unresolved image. Note that although the mass distribution is discontinuous at the pixel boundaries, the lens equation is continuous.

2. For lenses with measured time delays, the model is

required to reproduce them. Concordance values of $H_0, \Omega_M, \Omega_\Lambda$ (i.e. 72 km s^{-1} Mpc^{-1},0.3,0.7) are assumed.

In addition, the mass distribution must satisfy the following prior conditions.

1. The local density gradient must point no more than 45° away from the centre of brightness. Since the central regions of galaxies are expected to be dominated by stars, it seems safe to assume that the mass and light peaks coincide.

2. The circular average (around the centre) of the projected density, falls off as $R^{-1/2}$ or faster. The three-dimensional mass profiles of galaxies are thought to be invariably steeper than $r^{-1.5}$, so again this appears to be a safe prior assumption.

3. No pixel is allowed to be more than twice the mean of its neighbours, except for the central pixel, which can be arbitrarily high to mimic central density cusps,

4. Unless the lens shows signs of asymmetry, the mass distribution is required to be symmetric under a 180° rotation around the centre.

In practice, there are infinitely many mass models that satisfy all the above conditions, because solutions of the lens equation are highly non-unique (Falco et al. 1985; Saha 2000; Liesenborgs et al. 2008). Accordingly, for each lens we generate an ensemble of 300 models, by a random-walk technique in model space. The random walk implicitly defines a prior measure in model space, and it turns out that an equivalent statement of the prior measure is that it must be invariant under rescalings of units (Coles 2008). A very useful property of the above constraints (observational or prior) is that they can all be formulated as linear equations or inequalities. This means any weighted mean of ensemble members is also an admissible model. Hence, we can conveniently use the ensemble mean to represent a typical model. However, the main results later in this paper use the full model ensembles.

The lens models do not attempt to subtract off lensing mass outside the galaxy. Such mass could come from the environment, 14 of the lenses being in dense environments (see column *env* in Tab. 1), or it could be in an interloper along the line of sight. However, given that the model-ensemble technique yields conservatively large error-bars on the mass maps, we expect that external lensing mass is unlikely to be larger than the estimated uncertainties.

In the following section, we will consider the circularly-averaged enclosed mass profile $M(< R)$, see Figures 3 and 4. The outermost radius to which the mass profiles are reconstructed is fixed to two times the lensing radius $R_{\rm lens}$, which is defined as the radial position of the outermost lensed image with respect to the center of the lens. We choose $2R_{\rm lens}$ as a trade-off between uncertainty and common radial range for the sample. The range of enclosed-mass profiles in the ensemble, which is interpreted as the uncertainty, has a characteristic butterfly shape. That is to say, $M(< R)$ is well constrained in the image region, but becomes more uncertain farther in or out. Note that the butterfly shape is less prominent or even distorted for less symmetric lensed image configuration. The steep limit of the butterfly shape is expected to be roughly $M(< R) \sim R^{1.5}$, resulting from the minimal steepness of $R^{-0.5}$ in the projected density. The shallow limit of the butterfly shape is given by the steepest model in the ensemble.

4. RADIAL DEPENDENCE OF STELLAR VERSUS TOTAL MASS

To compare the radial dependence of stellar and total mass, it is interesting to consider pairs of lenses with matching $M_L(< R)$ or with matching $M_s(< R)$. To illustrate, in Fig. 3 we show three pairs of galaxies with the following properties (see also Table 1):

1. small mass, matching $M_L(< R)$ profiles, differing $M_s(< R)$,

2. intermediate mass, matching $M_L(< R)$ profiles, differing $M_s(< R)$,

3. high mass, differing $M_L(< R)$ profiles, matching $M_s(< R)$.

The radial scale is $R/R_{\rm Ein}$ where $R_{\rm Ein}$ has been estimated from the pixelated mass maps. Error bars are 68% confidence from the population-synthesis models used for $M_s(< R)$ values. For $M_L(< R)$ we use error bars corresponding to 90% of the $M_L(< R)$ range of the model ensemble, as described in section 3.3. Note that the errors attached to $M_s(< R)$ and $M_L(< R)$ are correlated.

The matched pairs are, of course, only rough matches. Also, the $R_{\rm Ein}$ values are not the same for the matched pairs of galaxies. The angular radial scale is proportional not only to the enclosed mass but also to $(d_{LS}/(d_L d_S))^{0.5}$ (corresponding to $(d_L d_{LS}/d_S)^{0.5}$ for the physical Einstein radius), where the d's are the angular diameter distances between observer and lens (L), observer and source (S) and lens and source (LS). Latter distance ratio must be approximately equal to identify matching profiles. To enable comparison between scales we include $R_{\rm Ein}/R_{\rm e}$ in Table 1. With these caveats, we point out some interesting features.

Consider first the two low-mass lenses PG1115 and Q0047 (bottom panels, Fig. 3). While the total mass within $2R_{\rm lens}$ is very similar, the stellar mass of PG1115 rises only to 50% that of Q0047. The same qualitative behavior is seen if these two galaxies are compared using $R/R_{\rm e}$ rather than $R/R_{\rm Ein}$ as the radial scale. Nevertheless, these two low-mass lenses have $f_s \equiv M_s/M_L \gtrsim 0.17$ the range of high baryon fractions. Lenses within this range can consequently be referred to as high f_s lenses.

Comparing the two intermediate mass lenses B1030 and MG0414 in the middle panels of Fig. 3, we find that their cumulative total mass curves are very similar. However, the stellar mass of B1030 is just $\sim 30\%$ that of MG0414, independent of the radius. If we consider the stellar radial scale, we find that MG0414 has ~ 4 times the stellar mass of B1030. Their baryon fractions approach values from $f_s \approx 0.05$ (B1030) to $f_s \approx 0.17$ (MG0414) at the outermost radius to which we have estimates. In the intermediate mass range of our sample (roughly $5 \times 10^{11} M_\odot$ to $15 \times 10^{11} M_\odot$) MG0414 has

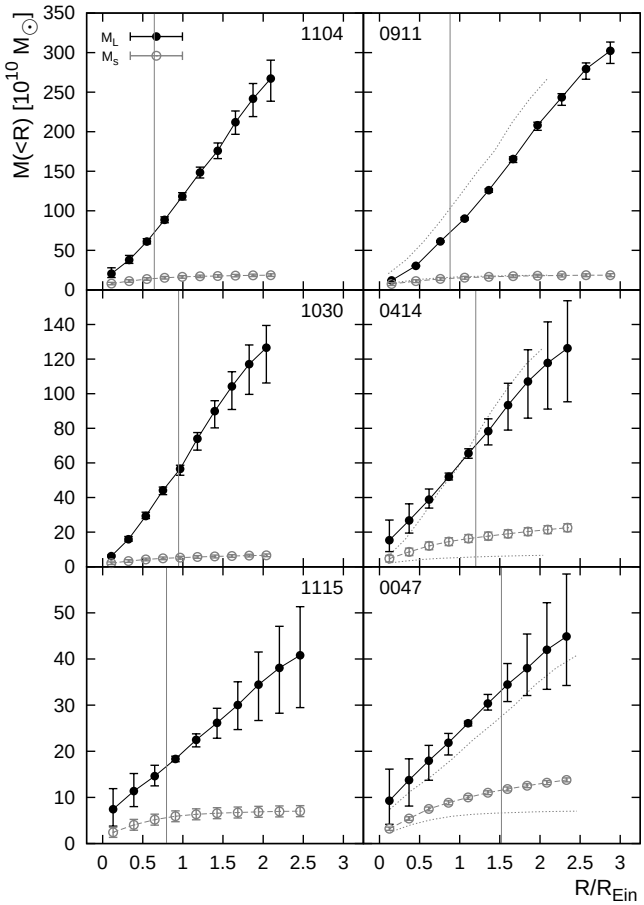

FIG. 3.— Cumulative stellar mass and lens mass profiles against projected radius (in units of the Einstein radius) for three comparable pairs of lenses. PG1115 and Q0047 (bottom row) are low mass, B1030 and MG0414 (middle) are intermediate mass, and HE1104 and RXJ0911 (top) are high mass. The gray vertical line marks $2R_{\rm e}$. To assist comparison, each right-hand panel has the profiles from the corresponding left-hand panel duplicated with thin dotted lines.

one of largest and B1030 the lowest stellar-mass fraction. It should be noted that the opposite behaviour, namely matching stellar profiles on both $R_{\rm lens}$ and $R_{\rm e}$ scale with very different total mass is also possible. An example for the latter would be a comparison between B1030 (middle row) and PG1115 (bottom row) of Fig. 3 with equal $M_s(R/R_e)$ but total mass profiles differing by a factor of 4.5 at $3R_{\rm e}$.

The two high mass lenses RXJ0911 and HE1104 have a total stellar mass of $\simeq 2\times10^{11}M_\odot$. For comparison, the total mass profiles differ slightly for radii $\lesssim 1.5R_{\rm e}$ and $\gtrsim 2.5R_{\rm e}$. But it should be noted that RXJ0911 is located at the centre of a galaxy cluster which might lead to a lens mass estimate slightly larger than the actual virial mass of the lens galaxy. At $6.5R_{\rm e}$, i.e., $\sim 2R_{\rm lens}$ HE1104 has 12% less total mass than RXJ0911. At $\sim 3R_{\rm e}$, i.e. $R_{\rm lens}$ the difference is still 6%. In terms of stellar-mass fraction HE1104 exhibits small values of $f_s \approx 0.07$ and RXJ0911 of $f_s \approx 0.06$. In the high mass regime ($> 15\times10^{10}M_\odot$) the range of possible stellar-mass fractions appears to be small compared to low and intermediate masses, and always close to 0.05. Those two lenses are thus representative for low f_s lenses.

Comparing lens profiles on $R_{\rm e}$ scales intrinsic to the luminous part of the galaxy, one can find many lenses with similar stellar mass profiles, which is not surprising. After all the enclosed mass values $M_s(<2R_{\rm lens})$ cover with $\sim 10^{10}$ to $\sim 2\times10^{11}$ a relatively small range in contrast to a total mass range $M_L(<2R_{\rm lens})$ of $\sim 2\times10^{10}$ to $\sim 2\times10^{12}$. However, pairs of lenses with matching $M_s(<R)$ and $M_L(<R)$ profiles over the whole radial range as shown in Fig. 4 are rare. Most lenses with matching $M_s(<R)$ profiles exhibit quite different $M_L(<R)$ profiles. The above lenses HE1104 and RXJ0911 are – apart from their data points $\gtrsim 6R_{\rm e}$ – matching pairs within uncertainties on $R_{\rm e}$ scale as they are on $R_{\rm lens}$ scale, a consequence of $R_{\rm lens}/R_{\rm e}$ being equal for both objects.

In Fig. 4 we present the left column lenses of Fig.3 now on baryonic scales, two of them have new counterparts with similar $M_s(<R)$ and $M_L(<R)$. As before we present low to high mass galaxies from the bottom up.

For the two low mass lenses PG1115 and B0712, we find that at their outermost common radius $\sim 2.5R_{\rm e}$ their baryon fraction is ~ 0.08. B1030 and BRI1009 also match well within their error bars although the mean stellar mass profile of B1030 is consistently below the one of BRI1009. The error region of its lens mass profile shows quite large error bars and thus make it easy to match. The baryon fraction at $2.7R_{\rm e}$ is approximately $f_s = 0.08$. If we compare lenses along the vertical direction of Fig. 4 B0712 and BRI1009 are representative for most lenses on low to high mass scales, that is, similar $M_s(<R)$, dissimilar $M_L(<R)$ and baryon fractions.

In summary we find on both baryonic scale $R_{\rm e}$ and lensing scale $R_{\rm lens}$:

- many pairs with the same enclosed total (lens) mass, but with different enclosed stellar mass,
- a small number of pairs (decreasing with increasing M_L) with the same enclosed total (lens) and stellar mass.

We can already conjecture an anti-correlation between enclosed lens mass and stellar-mass fraction, which will be studied in detail later on.

However, one should keep in mind that our result could be influenced by the lens environment and its history. See also Table 1, column '*Env*' and section 2 for information on the local lens environment. The phenomenon of same M_L but different M_s becomes less prominent for larger total lens masses, on both $R_{\rm lens}$ and $R_{\rm e}$ scale. Nevertheless, global trends and interdependencies might be revealed by analysing the whole set of lenses, which is done below.

Using our sample of 21 lensing objects we consider the following relations to highlight the interdependencies in the (M_L,M_s,R) parameter space:

1. the enclosed total mass $M_L(<R)$ as a function of enclosed stellar mass $M_s(<R)$ at a fixed radius R,
2. the stellar-mass fraction as a function of radial distance, $f_s(R) = M_s(<R)/M_L(<R)$,
3. the stellar-mass fraction as a function of the total mass M_L,

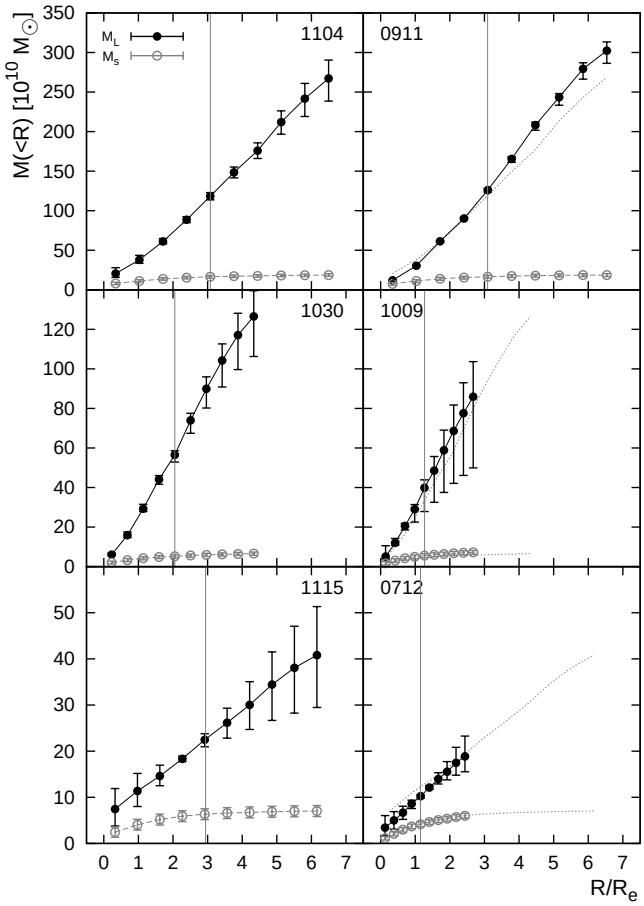

FIG. 4.— As in Fig. 3, but with the effective radius R_e as reference scale, shown for PG1115 and B0712 (bottom), B1030 and BRI1009 (middle), HE1104 and RXJ0911 (top). Here the grey vertical line marks $R_{\rm lens}$.

4. the stellar-mass fraction as a function of redshift.

Fig. 5 shows the first relation for a range of radial positions from $0.25R_e$ to $5R_e$, parametrized by the dimensionless quantity $x \equiv R/R_e$. For reference, we list in Table 1 the enclosed stellar and lens mass within $2R_e$ with error bars.

The universal baryon fraction according to WMAP5, $f_b = \Omega_B/\Omega_M = 0.17 \pm 0.02$ (Hinshaw et al. 2009), is included as two dashed lines for the upper and lower bounds. The solid line denotes a stellar-mass fraction of one, i.e. the total mass content consists of 100% stellar mass. Note that the data points refer to baryonic matter in stars and do not account for other baryonic content like gas and dust. The gas contents of our lens sample – mostly early type galaxies – is expected to be small. But for the Einstein Cross (Q2237), which is the bulge of a spiral galaxy, and B1600, which is likely to be a late-type galaxy viewed edge-on, one can indeed expect deviations from the obtained M_s values.

The galaxy B1608 shows an unreasonably high stellar-mass fraction for radii $\leq .75R_e$ (e.g. left panel in top row of Fig. 5). To take proper account of the light distribution we fit both the brightest galaxy and its merging companion with Sersic profiles, but we only use the information of the light profile of the brightest galaxy for the computation of stellar mass. The enclosed mass values are thus taken with respect to the center of the brightest galaxy. As a consequence of the degeneracy between the two Sersic profiles the central region of the light profile is modeled rather poorly. This causes an overestimate of the stellar content ($\lesssim 15\%$) in a region where the neighbouring galaxy, which is also responsible for light deflection, interferes with the fit. The pixels with highest total mass and highest stellar content do not match for B1608. This also causes larger deviations in the region $\lesssim 1R_e$.

The late-type galaxies Q2237 and B1600 might be subject to dust reddening. In general the impact of reddening on high redshift lenses is stronger due to the bluer populations observed in H-band and the higher absorption of dust at smaller wavelength. However, on the basis of the analysis shown in Appendix B, we do not expect departures of more than 20% towards higher M_s. This will shift $B1600$ closer to the bulk of lenses in Fig. 5.

The prominent f_s curve of B1422 — starting at twice the value of most other lens galaxies — might also be caused by light contamination. This time it originates from the innermost quasar image which lies just $0.25''$ away from the galaxy centre, an extreme among the 21 lenses studied in this paper.

In the online material of this paper we provide a movie version of Fig. 5 to help visualize the trend of the stellar-baryon fraction with increasing radius. See also Appendix A.

The lens galaxies reveal the following properties, which are qualitatively assessable already from Fig. 5, but will be explained in detail later on:

1. Most lenses populate a band of $0.1 < f_s < 0.4$ within $5R_e$.

2. The slope of the enclosed M_L-to-M_s relation of Fig. 5 within the shown radial range becomes gradually steeper for larger enclosed radii (an effect quantified in the following paragraph).

3. Between 2 (1.5) and $2.5R_e$ ($2R_e$) for most lenses with total mass below (above) $4\times10^{11}M_\odot$ the dark matter halos overtake the stellar content, that is they move primarily toward increasing total mass. The turning point thus depends on the halo mass. The dark matter halos of more massive galaxies start to dominate the matter balance at larger radii (in units of R_e) than those of less massive galaxies.

Note that by "overtake" we refer to the radius where $dM_L/dR \approx dM_s/dR$ rather than to the radius where the total stellar mass contributes 50% of the total mass. As a consequence of limited resolution this radius can only be given with larger uncertainties ($\sim 0.5R_e$).

Point 2 can also be illustrated by plotting the slope η determined from $M_s \propto M_L^\eta$ so that it represents light as a function of mass. We find that η asymptotically approaches 0.75, as one can see in Fig. 6, which is in agreement with previous studies of the fundamental plane within error bars (e.g., Guzman et al. 1993; Jørgensen et al. 1996; Leier 2009). A bootstrapping method for a large and a reduced sample is used to determine the M_s-to-M_L relation and its standard errors respectively. Both runs are done with 10^4 realizations. The 19-lens sample contains all the lenses except for

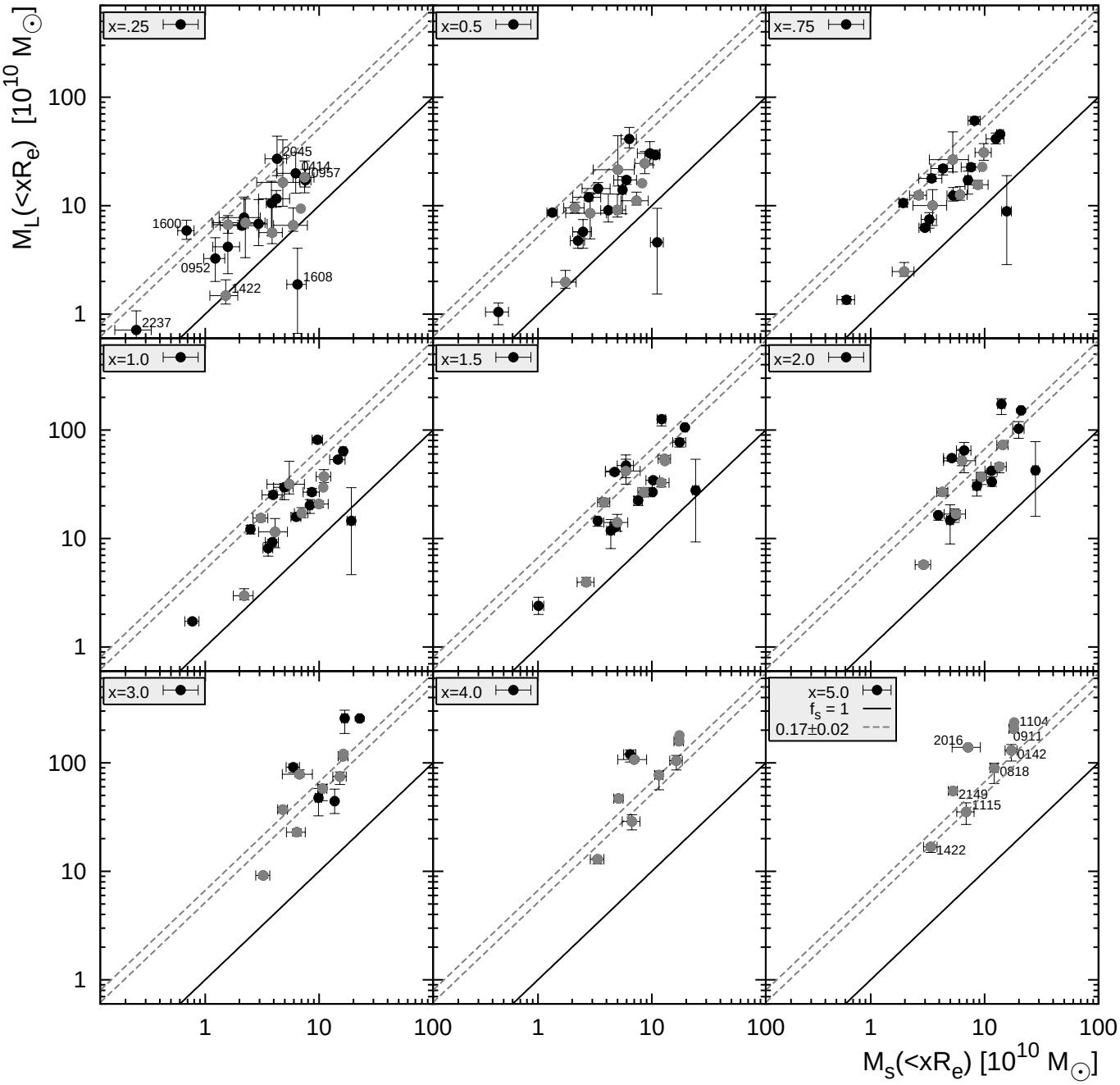

FIG. 5.— The panels show the enclosed M_L against enclosed M_s plane for a number of apertures, defined by the radial distance xR_e to the centre of the lens galaxy, labelled by 'x' in the top-left corner of each panel. We cover a radial distance from $0.25 \times R_e$ to $5 \times R_e$ from upper left to lower right panels in conveniently chosen steps. Grey circles highlight a subset of 8 lenses which are probed out to $5R_e$. The solid line denotes the equality of total and stellar mass, whereas the dashed lines represent the upper and lower limit of the global baryon fraction (Hinshaw et al. 2009).

the outlier B1608 and the late-type galaxy Q2237. Farther out in radius, the number of lenses with profiles extending to a particular radius decreases. Because of that, Fig. 6 also shows the number of lenses used for each fit. As a consequence of changing sample size discontinuities appear between 2.25 and $3.5R_e$ and at $4.5R_e$. The most extreme ones are caused by B0712 ($2.5R_e$) and B1030 ($4.5R_e$) falling out of the sample. The behaviour of the error bars in a bootstrap fit depends on the size of the drawn sample subset. To get more meaningful error bars we fixed the size of the sample subset to be 50% of the available number of lenses at each radius. The small sample instead comprises all 8 lenses being probed out to $5R_e$, which are highlighted in Fig. 5 by grey filled circles. From $M_s \propto M_L^{1.24\pm0.14}$ at $0.25R_e$ the reciprocal slope $\eta(R)$ declines as $1/R$ and ends up at $5R_e$ with the relation $M_s \propto M_L^{0.76\pm0.07}$. We expect only small deviations from this slope for larger radii since we run out of stars, and additional mass from the dark matter halo shifts the distribution upwards, whereas possible baryonic contributions from gas shift the whole population farther to the right of Fig. 5. Additionally, for the 19-lens sample a weighted best fit for $\eta(R)$ suggests that the function approaches

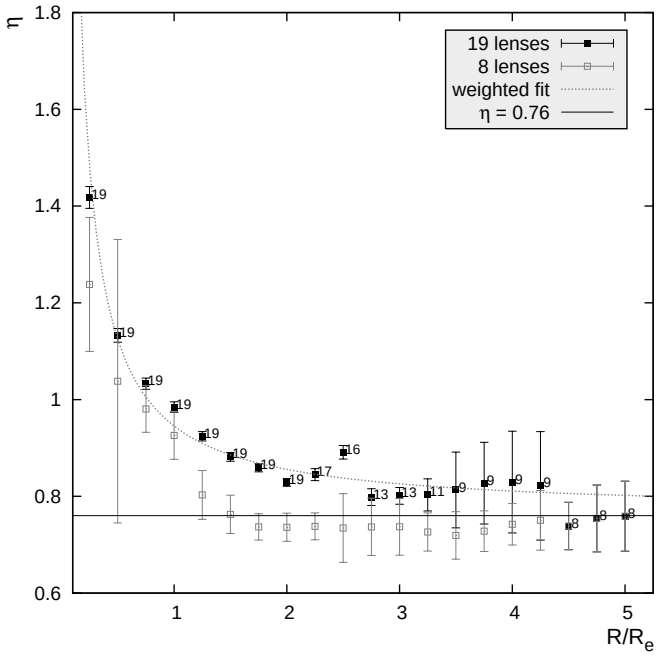

FIG. 6.— Slope of the M_s-to-M_L relation taken from Fig. 5 plotted against the distance to the centre in terms of effective radii. The median slopes are determined via a bootstrapping fitting method with 10^4 realizations to compute meaningful standard errors for a sample of 19 lenses (filled squares) and a reduced 8 lens sample (open squares). The numbers at the filled squares give the number of lenses probed out to the respective radius. The dotted line represents a weighted best fit of $\eta(R) \sim 1/R$+const.

asymptotically a constant value of 0.77 ± 0.01. Note that for the small sample $\eta(R)$ declines rapidly to reach the value of 0.76 already at $\sim 1.5R_{\rm e}$ and thereafter shows no significant departure from it. However, the change in slope from small to large radii is significant for both the 19-lens and the 8-lens sample.

All the stellar-mass fraction curves in the left and right hand panel of Fig. 7 turn over to a similar stellar-mass fraction between 1.5 and 2.5 $R_{\rm e}$, a fact also reflected by $\eta(R)$ in Fig. 6. With increasing radius, the stellar-mass fractions of high mass galaxies ($M_L(< 2R_{\rm e}) \gtrsim 4 \times 10^{11} M_\odot$) tend towards lower values in the majority of cases, meaning $f_s \lesssim 0.2$. Low mass galaxies ($M_L(< 2R_{\rm e}) \lesssim 4 \times 10^{11} M_\odot$) show a larger range of possible stellar-mass fractions at high and low radii, which are in a range between 0.1 and 0.35 (see left hand panel of Fig. 7). This is the reason for the large scatter of enclosed stellar-to-total enclosed masses at small radii in Fig. 5.

Averaged over the whole lens sample we find that the stellar-mass fraction declines with increasing radius from its value $f_s(< 1R_{\rm e})$ enclosed in $1R_{\rm e}$ to only $\sim 71\%$ of $f_{s,max}$ at $2R_{\rm e}$, $\sim 55\%$ at $3R_{\rm e}$, $\sim 39\%$ at $4R_{\rm e}$ and finally $\sim 33\%$ at $5R_{\rm e}$. Splitting the sample with respect to total mass as done before yields a different picture: For lenses with $M_L(< 2R_{\rm e}) \lesssim 4 \times 10^{11} M_\odot$ 79% of the stellar-mass fraction at $1R_{\rm e}$ remains at $2R_{\rm e}$, 63% at $3R_{\rm e}$, 47% at $4R_{\rm e}$ and finally 40% at $5R_{\rm e}$. For lenses with $M_L(< 2R_{\rm e}) \gtrsim 4 \times 10^{11} M_\odot$ 64% of the stellar-mass fraction at $1R_{\rm e}$ is found at $2R_{\rm e}$, 48% at $3R_{\rm e}$, 33% at $4R_{\rm e}$ and finally 27% at $5R_{\rm e}$. The uncertainties of stellar-mass fractions at $1R_{\rm e}$ for low M_L lenses are only as high as 10%. For larger radius and mass the f_s errors decline strongly to less than 1%. From this we can conclude the following.

1. Low mass galaxies show a shallower decline in their enclosed stellar-mass fraction than high mass galaxies: either their stellar content is less concentrated than in high mass galaxies or their dark matter content is more concentrated. This point becomes clearer in Section 5, where we calculate concentration indices of stellar and total mass profiles,

2. The relative stellar-mass fraction of high versus low mass galaxies is significantly offset by a constant value within $5R_{\rm e}$ from the centre, i.e.

$$\frac{f_s(< R)}{f_s(< 1R_{\rm e})}\Big|_{M_L > 4E11 M_\odot} \approx \frac{f_s(< R)}{f_s(< 1R_{\rm e})}\Big|_{M_L < 4E11 M_\odot} - 0.15 \quad (1)$$

for $2R_{\rm e} < R < 5R_{\rm e}$.

The latter phenomenon becomes more evident when plotting the stellar-mass fraction at fixed $R/R_{\rm e}$ against the total mass as in Fig. 8. From left to right the panels show the f_s–M_L relation at discrete radii of 0.5, 1.0, 2.5 and 4.0 $R_{\rm e}$. It should be emphasized that the solid line fit does not imply a physical relation extendable to the high or low mass end of the plot. Note that the relation has a tendency to steepen gradually towards lower radii whereas the scatter increases. Comparing this to recent results from Guo et al. (2010) where the ratio of total enclosed stellar mass and halo mass $M_{\rm halo}$ is analyzed with an abundance matching method, we find that their stellar-mass fraction curve shows a peak at a halo mass of around $6 \times 10^{11} M_\odot$ and decreasing fractions towards lower and higher halo masses. This is overplotted in the last panel of Fig. 8.

The effective height of the curve f_b is reduced in contrast to our results owing to the fact that there is significant dark matter in the halo extending up to the virial radius, which is defined as

$$R_{\rm vir} = \left(\frac{G M_{\rm halo}}{100 H^2(z)} \right)^{1/3}. \quad (2)$$

$R_{\rm vir}$ is roughly a hundred times larger than the region probed in this study. We list $R_{\rm vir}$ values deduced from M_s of this study given their M_s-to-$M_{\rm halo}$ relation in Table 1, which has additional implications on the lens environment, provided that the lens behaves like an SDSS-Galaxy plus simulated halo counterpart of respective stellar mass. To visualize how the computed stellar-mass fractions change between our resolution range and the virial radius we multiply a constant factor by the stellar-mass fraction curve from Guo et al. (2010) and divide its total mass by the same factor (here we use 5). The slope of the high mass end of their curve agrees with our best fit of $M_L^{-0.16 \pm 0.04}$ within error bars. Scaling to lower radii makes the mismatch for lower M_L even more prominent. However, we conclude that down to a certain level the M_s-to-$M_{\rm halo}$ from Guo et al. (2010) is scalable. In the $5R_{\rm e}$-to-$R_{\rm vir}$-range, the lower-mass lensing galaxies need to decrease their stellar-mass

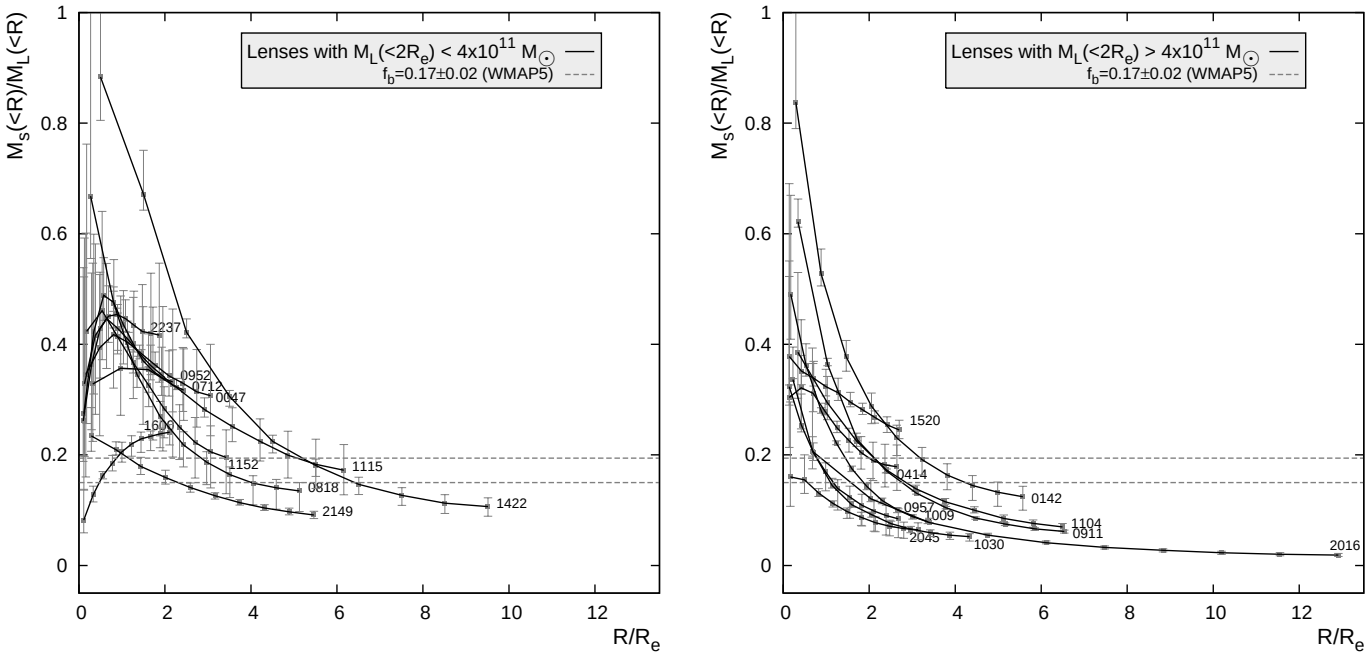

FIG. 7.— Left panel: Stellar-mass fraction against radius in effective radii for lenses with lens mass enclosed within $2R_e$ below 4×10^{11} $M_\odot$. Right panel: Similar, but for lenses with $M_L(< 2R_e)$ above 4×10^{11} $M_\odot$.

fractions by a larger amount than high mass galaxies in order to match with the results from Guo et al. (2010). Note that scaling our lens sample instead towards higher total masses and lower stellar-mass fractions yields the same result.

We should point out that this direct comparison of our results with Guo et al. (2010) is imperfect, since $M_{\rm halo}$ and M_L are differently defined and the spatial distribution of dark matter in a region not directly addressed in either paper is unknown. On the other hand the steepest part of the total mass profiles is already enclosed and the cumulative mass profiles saturate, i.e. the slope of the M_L-to-f_s relation is only slowly changing beyond $5R_e$. These different trends for f_s at lower masses could be indicative of an underestimated stellar-mass fraction towards smaller halo masses or an overestimated baryonic content towards higher halo masses. If the aforementioned study of the f_s-to-M_L dependency is correct, then our findings give rise to the question of what makes the stellar-mass fraction of low mass galaxies decline less strongly within $5R_e$ than in the range from $5R_e$ up to the virial radius, in contrast with high mass galaxies. Expressed in terms of stellar mass content we find a steeper decrease of stellar-mass fractions towards larger M_s than our results predict.

The above defined virial radius $R_{\rm vir}$ becomes smaller for lower stellar mass content. Low M_s galaxies reside in halos with larger f_s than high M_s galaxies, meaning the mass in the dark matter halo relative to M_s is even larger, i.e. small galaxies have more concentrated dark matter halos than larger ones (see also Section 5).

In order to investigate the influence of the distance/lensing-bias, we also show the redshift dependence of the stellar-mass fraction in Fig. 9. The ordinate might be subject to several biases. The lensing galaxies plus halo must be massive to produce an observable signature. The galaxy should not be too faint to be seen and has to obey our selection criterion of sufficient separation from quasar image. Fig. 9 shows that the correlation between stellar-mass fraction and redshift becomes more pronounced with larger radius. However, the strongly increasing scatter below $4R_e$ blurs the correlation and the slope shows no uniform trend.

5. DIAGNOSTICS OF BARYON COOLING

We now consider two different measures of the stellar and total-mass profiles, with a view to gaining insight on the evolution of lens galaxies from formation to observation redshift.

5.1. *Concentration index*

Our spatially resolved stellar and total mass maps allow us to study the difference in concentration of the baryon and the total mass distribution. We define a concentration index (see e.g. Bershady et al. 2000) as $c \equiv R90/R50$, where $R90$ and $R50$ denote the radii enclosing 90 and 50 percent of the mass (either stellar or lens mass). For the luminous component, a concentration index above 2.6 indicates an early-type galaxy, whereas indices below 2.6 refer to late-type galaxies(see e.g. Fig. 1 in Ferreras et al. 2005). Previous studies based on the surface brightness distribution use the Petrosian radius (or a given number of Petrosian radii) to define the total brightness. In our case, we redefine c and take the respective radii of our cumulative stellar mass and total mass profiles instead — 100% corresponding to enclosed masses at $2R_{\rm lens}$ (except for Q0957 and HS0818 where it is $1.5R_{\rm lens}$). In Fig. 10 we show concentration versus redshift in the left-hand panel with no obvious correlation and the frequencies per concentration bin in the right-hand panel. Note that defining the concentration values using $R_{\rm Ein}$ instead of $R_{\rm lens}$ will change the concentration values slightly, but even for $R_{\rm lens}/R_{\rm Ein} = 1.5$ we obtain changes in the lens mass concentration of less than $\sim 30\%$ and only for lenses with high concentrations.

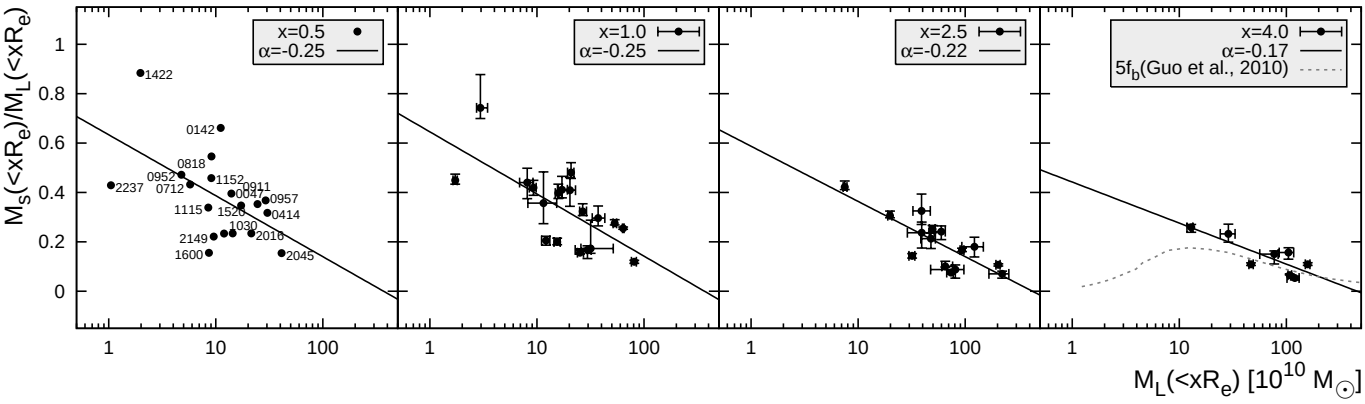

FIG. 8.— The stellar-mass fraction determined at 0.5, 1.0, 2.5 and 4.0 R_e against total mass. The best fits are found for the sample excluding lenses with mean stellar-mass fractions above 1 at R_e, which is the case only for B1608.

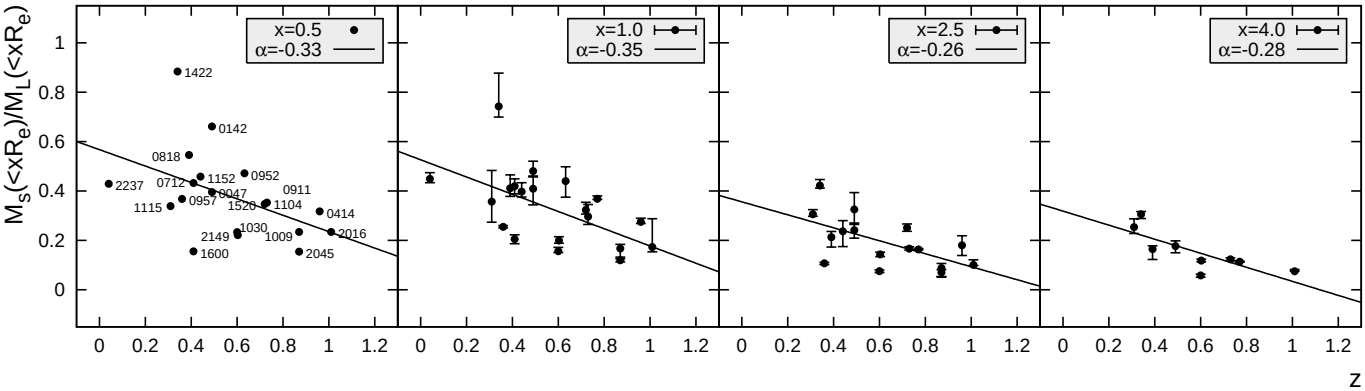

FIG. 9.— The stellar-mass fraction determined at 0.5, 1.0, 2.0 and 4.0 R_e against redshift.

From Fig. 10 the frequency distribution of c_{M_s} peaks between 3.0 and 3.5 which is in agreement with most concentration studies of early-type galaxies (e.g. Yamauchi et al. 2005; Deng et al. 2010). That is, even with the redefined concentration quantities one can distinguish the lens galaxies morphologically. Evidence is given by the two late-type galaxies Q2237 and B1600 which indeed lie below 2.6. For the two merging galaxies in the lens B1608, the interfering potential (for c_{M_L}) or light (for c_{M_s}), causes the concentration values to be decreased, pushing c_{M_s} down to 2.6. For the same reason we obtain rather large error bars on the lens mass.

One could check in detail now if the strong correlation between c and Hubble-type is maintained for the newly defined c_{M_s}. If we define a concentration parameter by means of the total mass profiles we expect, as our findings in Section 4 already suggest, a totally different distribution. Most lenses exhibit c_{M_L} values in a narrow region between 1.5 and 2. However, neither in c_{M_s} nor in c_{M_L} can a clear evolutionary trend be found. Figure 11 shows that the concentration parameter for stellar mass c_{M_s} has a rising trend with total lens mass, whereas c_{M_L} clearly declines with lens mass.

Note that the error bars of c_{M_s} and c_{M_L} are the standard errors of the $R90/R50$ values of each model in the ensemble multiplied by student's t for a 95% confidence interval. This was done since the ensemble can be seen as being part of a normal population. The horizontal error bars are the M_L errors at the outermost radius of the reconstructed mass profile. As we can see at low total lens masses the distributions of M_s and M_L are almost the same, which means that the M_L profile approaches the distribution of the baryonic matter. An interaction between the baryonic and dark matter distribution seems to be a reasonable explanation, since already in Section 4 we find that the stellar-mass fractions of less massive lenses are larger than for the more massive lenses.

A possible interaction between baryons and dark matter is likely to influence the slope of the total mass distribution close to the center of galaxies. If we assume a density following a pure power law $\rho(r) \sim r^{-\beta}$ the enclosed mass becomes $M(< R) \sim r^{3-\beta}/(3-\beta)$. Thus the concentration c and the density slope obey the relation

$$\beta = 3 - \frac{\ln 0.9/0.5}{\ln c}. \quad (3)$$

Figure 12 contrasts the relation between β and c based on a pure power law (solid line) and data for different radial extents. The β values represent weighted best fits to lens mass profiles with standard errors from the fit. If the mass distribution does not follow a pure power-law ($R90/R50$) might depend strongly on the radial extent of the lens ($2R_{\rm lens}$). Therefore we compare in both panels of Fig. 12 concentration values inferred from differently sized profiles, with a maximal radius of $1R_{\rm lens}$ and $2R_{\rm lens}$. The innermost data point has rather large uncertainties and deviates in most cases strongly from the trend at larger radius. To demonstrate its impact on the relation we contrast fits with (left panel) and without (right panel) regard of the innermost point. According

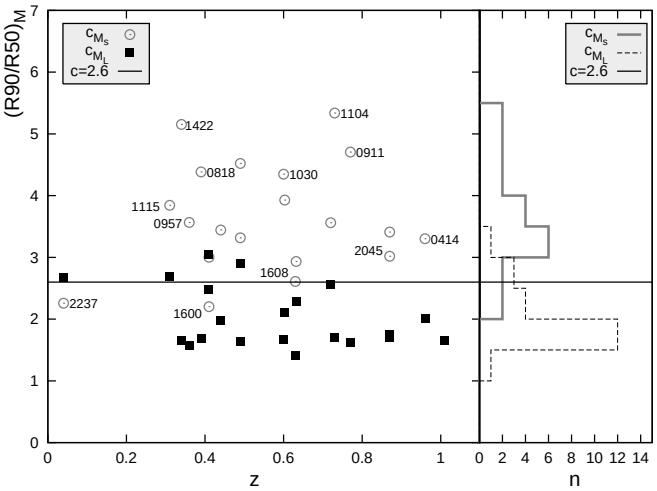

FIG. 10.— Concentration index $c = R90/R50$ versus redshift, where c is the ratio of the radii enclosing 90% and 50% of the total stellar mass (c_{M_s}, open circles) and lens mass (c_{M_L}, filled squares). For MG2016 R50 cannot be calculated due to lack of data points at small radii. The solid line indicates $c = 2.6$ separating early-type ($c > 2.6$) from late-type galaxies ($c < 2.6$). Error bars for index c can be found in Fig. 11.

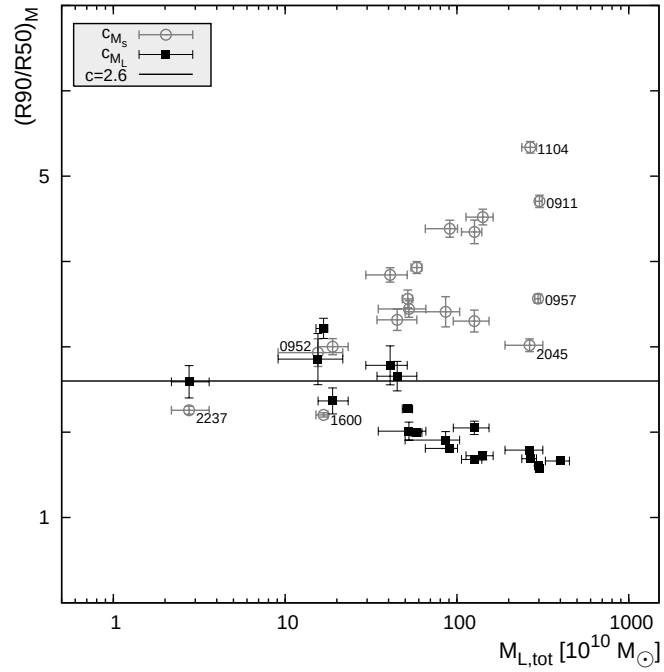

FIG. 11.— As in Fig. 10 but plotted against the total mass $M_{L,tot}$ enclosed in $2R_e$. The y-axis error bars represent for c_{M_L} the standard errors for mean concentrations of 300 models. For c_{M_s} the error bars correspond to the uncertainties originating from a 10% error in the flux per pixel.

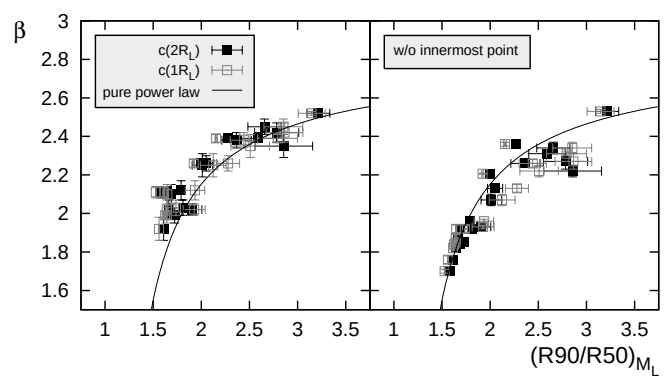

FIG. 12.— Power law index β of the density profile plotted against the concentration parameter $c = (R90/R50)_{M_L}$ for the total lens mass distribution. Filled (open) squares indicate $c = (R90/R50)_{M_L}$ determined for a profile extending to $2R_{\rm lens}$ ($1R_{\rm lens}$). The left panel uses power law fits to the whole radial range, whereas the right panel neglects the innermost data point. The solid black line shows the pure power law case according to eq. 3.

to eq. 3 we find that with increasing $M_L(< 2R_e)$ – i.e. decreasing concentration – the slope β gets shallower. It is remarkable how extraordinarily well the weighted power law fits neglecting the innermost point reproduce the simple $\beta(c)$ model at low concentrations, but fail to do so at large concentrations, where the data lies below the pure power law relation. Higher values of β correspond to shallower M_L profiles. Including the innermost point always flattens $M_L(< R)$ fits, which explains why respective β values, although less representative for the outer part of the profiles, are in better agreement with eq. 3. We can conclude that

1. excluding the core region of the lenses, we obtain power law indices and concentration parameters ($R90/R50$) indicative of a pure power-law behaviour for small concentrations. This notion is strengthened by only small shifts of ($R90/R50$) going from 2 to $1R_{\rm lens}$ profiles.

2. For more concentrated total mass distributions, we find evidence for a significant departure from pure power law behaviour. This is confirmed by significant shifts of ($R90/R50$) while reducing the extent of the lens from 2 to $1R_{\rm lens}$ and an increasing β error towards higher concentrations.

5.2. *Energy ratio*

By means of the stellar mass content one can approach the subject of galaxy formation from a different viewpoint. The first question is: "is it feasible to determine a characteristic quantity which gives us the amount of energy lost between the collapse of an initial sphere of homogeneously distributed baryons and its later state as a lens galaxy?". One could ask as well for a ratio of the radius of the pre-collapse sphere and an observable spatial quantity, like the effective radius. Even though this is a rough estimate, one can gain insight in the evolution process of galaxies.

At the time of collapse t_1, a region decouples from the expansion of the surrounding universe. The baryons which are assumed to be homogeneously distributed in this sphere are for now assumed to make up the whole stellar content of the later lens galaxy, neglecting any kind of active evolution such as caused by mergers, ram pressure, tidal stripping, etc. The radius r_1 of such a sphere at t_1 is

$$r_1 = \left(\frac{M_s}{\frac{4}{3}\pi \Omega_b \rho_c} \right)^{1/3} (1+z_1)^{-1} \qquad (4)$$

where $\Omega_b = 0.0441 \pm 0.0030$ is the baryonic energy density in terms of critical density according to Hinshaw et al.

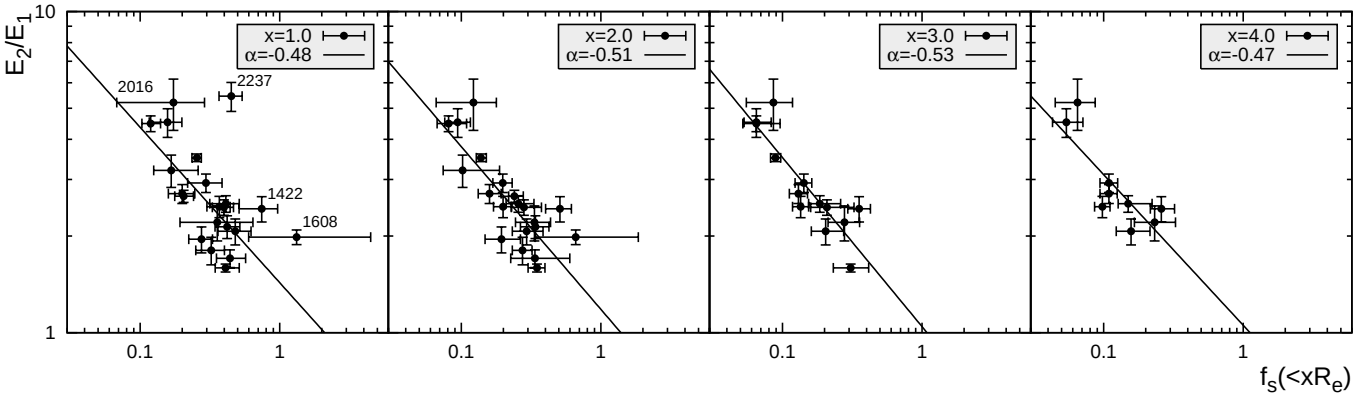

FIG. 13.— The stellar-mass fraction determined at 1.0, 2.0, 3.0 and 4.0 R_e versus E_2/E_1. The solid line denotes the best fit of a power-law with slope α. The fits exclude Q2237 and MG2016.

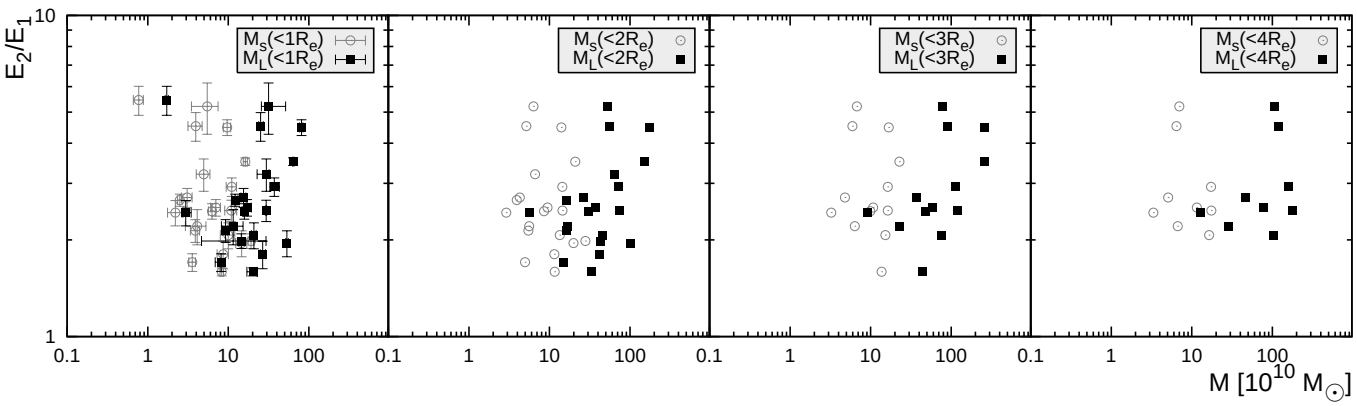

FIG. 14.— The energy ratio versus enclosed stellar and enclosed total mass at 1.0, 2.0, 3.0 and 4.0 R_e.

(2009) and $\rho_c \simeq 143.87 M_\odot/\mathrm{kpc}^3$. The average Newtonian energy per unit mass at t_1 consists only of the potential energy per unit mass, which is

$$E_1 = -\frac{GM_{\rm tot}}{r_1}. \tag{5}$$

The total mass $M_{\rm tot}$ is defined here as

$$M_{\rm tot} = \Omega_m \rho_c (1+z_1)^3 \frac{4}{3}\pi r_1^3 \tag{6}$$

As the collapse goes on the baryons start to fall in to build a more tightly bound structure. At the observation redshift, i.e. at time t_2, we find mostly objects which are in virial equilibrium, that is $E = -T$, where T denotes kinetic energy. Thus we can determine the total energy per unit mass of the galaxy at t_2 to be

$$E_2 = -T_2 = -\frac{1}{2}\sigma_{\rm lens}^2, \tag{7}$$

where

$$\sigma_{\rm lens} \equiv \sqrt{GM_L(<R)/R} \tag{8}$$

is an effective velocity dispersion inferred from lensing (see Table 1). It is computed at $R = R_{\rm lens}$ and assumed not to vary drastically with radius. This effective dispersion has been shown to be an appropriate surrogate for the observed kinematic velocity dispersion (Leier 2009). Thus,

$$\frac{E_1}{E_2} = \frac{2GM_{\rm tot}}{\sigma_{\rm lens}^2 r_1} = \frac{G\Omega_m\rho_c(1+z_1)^3\frac{8}{3}\pi r_1^2}{\sigma_{\rm lens}^2} \tag{9}$$

using Eq. 4,

$$\frac{E_2}{E_1} \propto \frac{\sigma_{\rm lens}^2}{M_s^{2/3}}. \tag{10}$$

Thus we get a quantity $E_1/E_2 \propto R_{\rm lens} \times M_s^{2/3}/M_L$ or $R_{\rm lens} M_s^{-1/3} f_s$. This is reminiscent of the Kormendy relation, except that it relates to three-dimensional rather than projected densities. For definiteness, we assume a formation redshift $z_1 = 5$, but the value only implies a multiplicative constant. Plotting the energy ratio against the stellar-mass fraction, we find a strong correlation (Fig. 13) regardless of the enclosure radius. The slope changes only marginally, but the scatter decreases with increasing radius.

However, E_2/E_1 appears to be uncorrelated with the enclosed stellar and total mass. For different radii one obtains Fig. 14. The fact that E_2/E_1 exhibits such a tight correlation with f_s but no clear correlation to contributing masses, can be interpreted as insensitivity of the star formation in early-type galaxies to active evolution processes over the time span from z_1 to $z_{\rm lens}$.

6. DISCUSSION

A resolved, model-independent and thus non-degenerate (w.r.t. M_s and M_L for fixed f_s) estimate of stellar versus total mass within galaxy halos is crucial to constrain current galaxy formation models and prescriptions of baryon-dark matter interactions used therein. Besides dynamical methods to explore scales below 10

kpc the combination of strong gravitational lensing and population synthesis used in this paper is most promising to give robust estimates of stellar-mass fractions.

The analysis of the radial dependence of the mass profiles of 21 CASTLES lenses presented in this paper allows us to draw the following conclusions. The relation between basic galaxy properties, i.e. M_L, M_s and $R_{\rm lens}$ cannot simply be scaled with their mass. The scatter in this parameter space turns out to be especially large for galaxies of smaller size. The study of M_s versus M_L and of the stellar-mass fractions ($f_s \equiv M_s/M_L$) enables us to discriminate between lens galaxies below and above $M_L(< 2R_{\rm e}) = 4 \times 10^{11} M_\odot$. The high mass class populates a lower and narrower f_s regime (0.05 to 0.2) on given scales and runs out earlier of stellar mass (i.e. at lower enclosed radius) than low mass lenses. The latter exhibit a more inhomogeneous behaviour with a wider range in f_s (0.1 to 0.5) and respective slopes.

We conclude that between 1.5 and $2.5R_{\rm e}$ dark matter halos start to dominate the matter balance depending on their total mass. This M_L-dependence causes high mass galaxies to gain mass primarily in the form of dark matter already at lower radii than low mass galaxies. Therefore the slope of the mass-to-light relation, which is a projection of the fundamental plane — or our equivalent representation, $M_L^\eta \propto M_s$ — becomes shallower with increasing radius and asymptotically approaches a slope of $\eta = 0.76 \pm 0.07$. Thus the FP tilt can be recovered as a gradually growing process with radius. Equivalently, the stellar-mass fraction shows a strong correlation to the total mass. As we contrast $f_s(M_L)$ with a comparable curve deduced by abundance matching from Guo et al. (2010) dissimilarities for low M_L galaxies become more evident the smaller the enclosed region gets. This is likely to be a result of different halo definitions, physical properties and processes, like baryon-dark matter interactions and adiabatic contraction which is beyond the scope of the aforementioned study. However, the f_s-to-$M_{\rm halo}$ relation scaled down to $4R_{\rm e}$ agrees quite well with lenses with $M_L \sim 10^{12} M_\odot$, since the biggest part of stellar matter is still enclosed.

Another important result of this study addresses the concentration of stellar (c_{M_s}) and total (c_{M_L}) mass profiles. The rule-of-thumb delimiter of $c = 2.6$ which separates early-type galaxies ($c > 2.6$) from late-types $c < 2.6$) holds also for the concentration parameter (c_{M_s}) defined by means of stellar mass instead of luminosity. In the low mass regime $M_L(< 2R_{\rm e}) \lesssim 4 \times 10^{11} M_\odot$ both, c_{M_s} and c_{M_L}, tend to similar values around 2.6. This means that the total mass profile is likely to be influenced by the distribution of baryonic matter in stars. From $10^{11} M_\odot$ upwards, c_{M_s} and c_{M_L} diverge, due to a stronger confinement of stars in more massive dark matter halos. The c_{M_L} values above $4 \times 10^{11} M_\odot$ stay around ~ 2 instead. Studying the interdependency of density slope and c_{M_L} we find that the reconstructed lens profiles show deviations from a pure power-law mass model, which is evidence for the sensitivity to the radial trends of the dark matter distribution.

The results presented in this paper are critical to ongoing studies about the reliability of parametric lens models and prescriptions used in galaxy-formation models. The radially resolved stellar to dark matter fractions should thus also serve as benchmarks for future simulations.

ACKNOWLEDGMENTS

We would like to thank the anonymous referee for comments that helped to improve this paper.

APPENDIX

ANIMATED RESULTS

An animated version of Fig. 5 is provided in the online material of this paper. The movie contains three panels. The left panel shows the enclosed M_L against enclosed M_s plane depending on the size of the aperture, defined by the radial distance $xR_{\rm e}$ to the centre of the lens galaxy. The solid black line denotes the equality of total and stellar mass, whereas the dashed lines represent the upper and lower limit of the global baryon fraction (Hinshaw et al. 2009). The upper right panel shows the lens PG1115 which is highlighted by a red label in the left panel. The lower right panel shows stellar baryon fraction versus radius as in Fig. 7. The solid black line denotes the baryon fraction curve of PG1115. With each time step of the movie the enclosure radius increases indicated by the factor x in the legend of the left panel and the red lines in the two right-hand panels. We cover a radial distance from 0.125 $R_{\rm e}$ to 5 $R_{\rm e}$ in 40 time steps.

DUST REDDENING

In this section we study the impact of dust reddening. Fig. 16 shows what happens when dust is included in the analysis of two lenses where the contribution of dust could be important: B1600 and B1608. For this exercise we take a simpler set of models, but the underlying effect from dust is similar to the more complex case involving exponentially decaying star formation histories. We run a set of simple stellar populations with solar metallicity, changing the age and the dust content. The models are reddened according to a single parameter $E(B-V)$ – that follows a Galactic reddening curve (e.g. Fitzpatrick 1999), assuming R$\equiv A_V/E(B-V) = 3.1$ (other reddening laws will not introduce significant differences). The observed V–i and i–H colours constrain the stellar M/L in the observed H band, which is used to determine the stellar mass content, following the standard methodology of this paper. The panels, from top to bottom, show the best SSP-based luminosity-weighted age, stellar mass, and χ^2 as a function of the reddening parameter $E(B-V)$. We find that dust "conspires" with age such that an increase in dust is compensated by a

Lens	z_L	z_s	$\Delta\theta$ [$''$]	$\Delta\theta$ [kpc]	R_e [$''$]	$\frac{R_{lens}}{R_e}$	$\frac{R_{Ein}}{R_e}$	$M_L(<2R_e)$ [$10^{10}M_\odot$]	$M_s(<2R_e)$ [$10^{10}M_\odot$]	$\frac{M_s}{L_V}$ [$\frac{M_\odot}{L_\odot}$]	σ_{lens} [km s^{-1}]	R_{vir} [kpc]	*Env*
Q0047	0.485	3.60	2.20	12.82	0.880 ± 0.025	1.45 ± 0.04	$1.31^{+0.02}_{-0.01}$	$33.27^{+3.80}_{-3.03}$	11.58 ± 0.43	$5.04^{+1.09}_{-0.89}$	$189.2^{+5.7}_{-4.8}$	538.4	G(9)
Q0142	0.490	2.72	2.23	13.10	0.703 ± 0.013	2.64 ± 0.05	$2.54^{+0.70}_{-0.83}$	$45.81^{+3.31}_{-5.50}$	13.45 ± 2.05	$2.92^{+0.90}_{-0.69}$	$245.8^{+16.8}_{-46.8}$	666.5	-
MG0414	0.960	2.64	2.08	16.01	0.734 ± 0.018	1.85 ± 0.05	$1.67^{+0.09}_{-0.07}$	$102.76^{+16.55}_{-19.04}$	19.90 ± 2.29	$5.62^{+2.27}_{-1.62}$	$247.0^{+9.93}_{-12.9}$	635.0	1
B0712	0.410	1.34	1.29	6.82	0.702 ± 0.016	1.15 ± 0.03	$1.02^{+0.05}_{-0.02}$	$16.13^{+2.55}_{-2.04}$	5.46 ± 0.52	$3.27^{+0.62}_{-0.52}$	$164.1^{+6.73}_{-6.78}$	295.8	1
HS0818	0.390	3.21	2.56	13.15	0.679 ± 0.013	3.27 ± 0.06	$2.51^{+0.55}_{-0.70}$	$36.88^{+3.69}_{-5.48}$	9.44 ± 0.97	$5.42^{+1.11}_{-0.92}$	$245.8^{+16.9}_{-41.8}$	517.8	1
RXJ0911	0.769	2.8	3.22	23.16	0.725 ± 0.011	3.09 ± 0.05	$2.27^{+0.09}_{-0.14}$	$73.04^{+1.15}_{-1.36}$	14.52 ± 1.87	$2.99^{+1.00}_{-0.75}$	$278.6^{+3.9}_{-6.0}$	590.4	C
BRI0952	0.632	4.5	0.99	5.27	0.619 ± 0.021	1.04 ± 0.04	$0.82^{+0.32}_{-0.13}$	$14.76^{+5.67}_{-5.87}$	4.98 ± 0.35	$2.78^{+0.64}_{-0.52}$	$140.0^{+15.8}_{-20.6}$	233.5	G(5)
Q0957	0.356	1.41	6.17	29.98	1.491 ± 0.018	3.51 ± 0.04	$2.39^{+0.14}_{-0.20}$	$151.29^{+5.17}_{-6.58}$	20.92 ± 0.96	$2.52^{+0.62}_{-0.50}$	$374.6^{+11.9}_{-14.0}$	950.0	C
LBQS1009	0.880	2.74	1.54	11.56	0.963 ± 0.028	1.27 ± 0.04	$1.07^{+0.18}_{-0.38}$	$64.73^{+11.97}_{-24.46}$	6.62 ± 0.96	$2.14^{+0.86}_{-0.61}$	$220.9^{+17.8}_{-65.6}$	252.1	-
B1030	0.600	1.54	1.32	8.60	0.675 ± 0.019	2.05 ± 0.06	$2.11^{+0.36}_{-0.33}$	$55.09^{+2.11}_{-3.52}$	5.16 ± 0.80	$1.12^{+0.32}_{-0.25}$	$256.8^{+9.9}_{-17.9}$	277.2	1
HE1104	0.730	2.32	3.19	22.54	0.681 ± 0.010	3.08 ± 0.05	$3.11^{+0.32}_{-0.25}$	$72.80^{+3.68}_{-3.22}$	14.43 ± 1.62	$3.50^{+1.04}_{-0.80}$	$302.9^{+11.9}_{-11.0}$	604.5	-
PG1115	0.310	1.72	2.43	10.76	0.478 ± 0.009	2.94 ± 0.06	$2.50^{+0.22}_{-0.13}$	$16.80^{+1.31}_{-1.23}$	5.61 ± 1.19	$3.68^{+1.23}_{-0.92}$	$191.6^{+11.7}_{-12.9}$	354.0	G(13)
B1152	0.439	1.02	1.56	8.60	0.691 ± 0.013	1.62 ± 0.03	$1.43^{+0.41}_{-0.25}$	$30.43^{+4.23}_{-5.86}$	8.57 ± 0.65	$2.84^{+0.61}_{-0.50}$	$216.9^{+22.8}_{-37.6}$	431.4	-
B1422	0.337	3.62	1.29	6.02	0.241 ± 0.003	4.49 ± 0.06	$3.56^{+0.23}_{-0.43}$	$5.72^{+0.39}_{-0.24}$	2.91 ± 0.45	$6.40^{+1.21}_{-1.02}$	$162.9^{+4.9}_{-11.9}$	231.3	G(17)
SBS1520	0.710	1.86	1.57	10.97	0.947 ± 0.018	1.28 ± 0.02	$0.95^{+0.08}_{-0.07}$	$41.98^{+1.49}_{-1.82}$	11.49 ± 1.41	$2.63^{+1.14}_{-0.79}$	$198.3^{+7.2}_{-9.1}$	434.3	G(4)
B1600	0.420	1.59	1.38	7.45	1.015 ± 0.007	1.00 ± 0.01	$0.75^{+0.05}_{-0.07}$	$16.38^{+0.82}_{-1.67}$	3.93 ± 0.17	$6.37^{+1.86}_{-1.44}$	$154.4^{+6.1}_{-12.1}$	236.0	G(6)
B1608	0.630	1.39	2.10	13.92	0.839 ± 0.047	1.82 ± 0.01	$1.55^{+0.12}_{-0.20}$	$42.49^{+35.50}_{-26.52}$	27.99 ± 1.63	$2.44^{+0.55}_{-0.45}$	$266.8^{+6.0}_{-14.9}$	972.9	G(8)
MG2016	1.010	3.3	3.36	26.22	0.406 ± 0.009	6.12 ± 0.14	$11.1^{+1.6}_{-2.8}$	$52.05^{+14.23}_{-5.13}$	6.34 ± 1.99	$0.89^{+0.40}_{-0.28}$	$308.6^{+9.9}_{-26.5}$	242.6	C(69)
B2045	0.870	1.28	1.93	14.46	0.950 ± 0.019	1.48 ± 0.03	$1.23^{+0.13}_{-0.15}$	$173.07^{+21.02}_{-34.20}$	14.05 ± 1.03	$2.47^{+0.62}_{-0.50}$	$338.8^{+16.6}_{-40.2}$	517.2	-
HE2149	0.603	2.03	1.71	10.02	0.531 ± 0.008	2.59 ± 0.04	$1.67^{+0.16}_{-0.23}$	$26.82^{+2.07}_{-2.19}$	4.28 ± 0.47	$0.79^{+0.20}_{-0.16}$	$191.2^{+7.1}_{-9.1}$	242.6	-
Q2237	0.039	1.7	1.83	1.40	1.090 ± 0.014	0.89 ± 0.01	$0.81^{+0.01}_{-0.01}$	$2.76^{+0.85}_{-0.58}$	1.15 ± 0.12	$4.39^{+1.76}_{-1.26}$	$145.2^{+3.8}_{-3.9}$	212.4	-

TABLE 1

Full set of gravitational lenses used for this analysis. All quantities in the table assume $H_0 = 72$ km s^{-1} Mpc^{-1}, $\Omega_m = 0.3$ and $\Omega_\Lambda = 0.7$. The underlined values show maximum and minimum. $\Delta\theta$ is the image separation. For systems with more than two images the maximal image separation between two images is given. Columns R_E, R_{LENS}/R_E and R_{EIN}/R_E contain Petrosian radii determined in the observed H-band with 1σ error bars. Note that R_{EIN} is computed from the critical surface density of the pixelated maps. The total and stellar masses enclosed within $2R_E$ are given in the following two columns. The stellar mass-to-light ratios in the rest-frame V-band are median values of all models. σ_{LENS} denotes the velocity dispersion at R_{LENS}. Column R_{VIR} gives the virial radius calculated using Eq. 2 and our stellar mass values in combination with the M_s-to-M_{halo} relation from Guo et al. (2010). The column labeled *Env* contains environmental information. "C" denotes a cluster environment, "G" a group environment and "1" a lens with only one known companion. If known the number of group members is given in parentheses. References for given values are mentioned in section 2. Colours and magnitudes are in agreement with comparable quantities in Rusin et al. (2003).

younger age to give the same colours, yielding a small variation of the estimated stellar mass with respect to dust reddening. Most importantly, the value of χ^2 worsens for high amounts of reddening. Hence we can safely say that even in the case of B1600 and B1608, the systematics on the stellar mass cannot be any larger than about 0.3 dex in $\log(M_s)$, shown as a shaded grey region in the middle panels of the figure. The other lens from our sample that could be affected by dust, Q2237 (i.e. the bulge of a late-type galaxy) is at a very low redshift ($z = 0.039$), so that stellar masses are determined from *rest-frame* H-band, which is even less sensitive to dust (Ferreras et al. 2010).

REFERENCES

Auger M. W., Fassnacht C. D., Abrahamse A. L., Lubin L. M., Squires G. K., 2007, Astron. J., 134, 668

Auger M. W., Fassnacht C. D., Wong K. C., Thompson D., Matthews K., Soifer B. T., 2008, Astrophys. J., 673, 778

Auger M. W., Treu T., Bolton A. S., Gavazzi R., Koopmans L. V. E., Marshall P. J., Moustakas L. A., Burles S., 2010, Astrophys. J., 724, 511

Bershady M. A., Jangren A., Conselice C. J., 2000, Astron. J., 119, 2645

Bower R. G., Benson A. J., Malbon R., Helly J. C., Frenk C. S., Baugh C. M., Cole S., Lacey C. G., 2006, Month. Not. Roy. Astr. Soc., 370, 645

Brooks A. M., Governato F., Booth C. M., Willman B., Gardner J. P., Wadsley J., Stinson G., Quinn T., 2007, Astrophys. J. Let., 655, L17

Bruzual G., Charlot S., 2003, Month. Not. Roy. Astr. Soc., 344, 1000

Buote D. A., Tsai J. C., 1995, Astrophys. J., 439, 29

Cappellari M., et al., 2006, Month. Not. Roy. Astr. Soc., 366, 1126

Chabrier G., 2003, The Publications of the Astronomical Society of the Pacific, 115, 763

Chartas G., Chuss D., Forman W., Jones C., Shapiro I., 1998, Astrophys. J., 504, 661

Claeskens J., Khmil S. V., Lee D. W., Sluse D., Surdej J., 2001, Astron. & Astrophys., 367, 748

Coccato L., et al., 2009, Month. Not. Roy. Astr. Soc., 394, 1249

Cole S., Aragon-Salamanca A., Frenk C. S., Navarro J. F., Zepf S. E., 1994, Month. Not. Roy. Astr. Soc., 271, 781

Coles J., 2008, Astrophys. J., 679, 17

Croton D. J., et al., 2006, Month. Not. Roy. Astr. Soc., 365, 11

Dekel A., Silk J., 1986, Astrophys. J., 303, 39

Deng X., Bei Y., He J., Tang X., 2010, Astrophys. J., 708, 101

Di Matteo T., Springel V., Hernquist L., 2005, Nature, 433, 604

Dunkley J., et al., 2009, Astrophys. J. Sup. S., 180, 306

Lens	Im.	Bands			PSF			fitting			masking			constraints		
		I	V	H	I	V	H	I	V	H	I	V	H	I	V	H
Q0047	4	✓	✓	✓	tt	tt	A(1030)	-	-	-	-	4P	-	-	-	-
Q0142	2	✓	✓	✓	it	tt	it	2P	1P	2P	-	1P	-	-	n	-
MG0414	4	✓		✓	tt		it	-		4P	4P		-	-		m
B0712	4	✓	✓	✓	tt	tt	tt	-	-	1P	4P	4P	3P	R_e	R_e	-
HS0818	2	✓	✓	✓	A	A	A(1030)	1P	1P	2P	B	B	-	-	PA	-
RXJ0911	4	✓		✓	it		it	4P		4P1S	-		-	n,$\underline{S}$		$\underline{xy}$
BRI0952	2	✓	✓	✓	it	it	it	2P	2P	2P	-	-	-	b/a	-	$\underline{b/a}$
Q0957	2+2	✓		✓	it		it	1P		2P	A		-	-		-
LBQS1009	2			✓			*(0414)			2P			-			n
B1030	2			✓			A			1P1S			1P			n
HE1104	2	✓		✓	A		*(0414)	1P		2P	-		-	b/a,PA		$\underline{xy}$
PG1115	4	✓	✓	✓	tt	it	it	-	-	4P	4P	4P	-	-	n	R_e
B1152	2			✓			A			1P1S			1P			-
B1422	4	✓	✓	✓	tt	tt	*(0414)	1P	1P	4P	3P	3P	-	R_e	R_e, b/a	b/a
SBS1520	2	✓		✓	it		*(1520)	2P		2P	1*		1*	R_e		$\underline{S}$
B1600	2			✓			A			2P			-			-
B1608	4	✓		✓	tt		*(0414)	1P1S		1P1S	3P		3P	R_e,$\underline{S}$		n, R_e,$\underline{S}$,$\underline{xy}$
MG2016	2+4	✓		✓	tt		*(0414)	-		1P1S	2P		1P2*	b/a		-
B2045	4	✓	✓	✓	tt	tt	*(2045)	-	-	1P	3P1b	3P	3P1b2*	-	-	n
HE2149	2	✓		✓	it		*(0414)	2P		2P	-		-	-		-
Q2237	4	✓	✓	✓	tt	tt	*(1654)	-	-	4P	4P	4P	-	$\underline{S}$	PA,$\underline{S}$	$\underline{S}$

TABLE 2

List of lens systems and how they were treated to obtain surface brightness profiles of the lens galaxies. From left to right the Lens-ID, the number of lensed images, the bands for which fitting was feasible, the PSF picking method, fitted and masked objects and necessary constraints are given. The column *PSF* includes the abbreviations *tt* for a PSF created with *TinyTim*, *A* for the outermost and thus fairly isolated quasar image, **(0414)* for an isolated star close to lens MG0414, *it* for the iteration method applied to the most isolated image and *A(1030)* for an isolated quasar image taken from lens B1030 used for subtracting quasar images and for the convolution of the whole image. In column *fitting* we summarize the number of objects, not significantly contributing to the lens mass, which are fitted with previously picked PSFs (P) and Sersic profiles (S). In column *masking* xP refers to a number of x masked out point sources, mostly quasar images, b denotes resolved but indistinct objects which are not necessarily connected to the lens mass and henceforth excluded from each fit. Point sources like foreground stars indicated by * are also masked out. A,B refer to quasar images which could be masked out given their separation from the lens galaxy. The last column states the type of constraint used if necessary to prevent each fit from diverging. The constrained parameters are: effective radius R_E, Sersic index n, axis ratio b/a, magnitude *mag*, position angle *PA*, sky background S and position of the Sersic profile xy. Parameters fixed at a certain value are underlined.

Eigenbrod A., Courbin F., Meylan G., 2007, Astron. & Astrophys., 465, 51
Eigenbrod, A. and Courbin, F. and Sluse, D. and Meylan, G. and Agol, E., 2008, Astron. & Astrophys., 480, 647
Falco E. E., Gorenstein M. V., Shapiro I. I., 1985, Astrophys. J. Let., 289, L1
Fassnacht C. D., et al., 1999, Astron. J., 117, 658
Fassnacht C. D., Gal R. R., Lubin L. M., McKean J. P., Squires G. K., Readhead A. C. S., 2006, Astrophys. J., 642, 30
Fassnacht C. D., Lubin L. M., 2002, Astron. J., 123, 627
Faure C., Alloin D., Kneib J. P., Courbin F., 2004, Astron. & Astrophys., 428, 741
Ferreras I., Lisker T., Carollo C. M., Lilly S. J., Mobasher B., 2005, Astrophys. J., 635, 243
Ferreras I., Lisker T., Pasquali A., Khochfar S., Kaviraj S., 2009, Month. Not. Roy. Astr. Soc., 396, 1573
Ferreras I., Saha P., Burles S., 2008, Month. Not. Roy. Astr. Soc., 383, 857
Ferreras I., Saha P., Leier D., Courbin F., Falco E. E., 2010, Month. Not. Roy. Astr. Soc., 409, L30
Ferreras I., Saha P., Williams L. L. R., 2005, Astrophys. J. Let., 623, L5
Fitzpatrick E. L., 1999, The Publications of the Astronomical Society of the Pacific, 111, 63
Gallazzi A., Bell E. F., 2009, Astrophys. J. Sup. S., 185, 253
Grant C. E., Bautz M. W., Chartas G., Garmire G. P., 2004, Astrophys. J., 610, 686
Guo Q., White S., Li C., Boylan-Kolchin M., 2010, Month. Not. Roy. Astr. Soc., pp 367–+
Guzman R., Lucey J. R., Bower R. G., 1993, Month. Not. Roy. Astr. Soc., 265, 731
Hagen H., Reimers D., 2000, Astron. & Astrophys., 357, L29
Häussler B., et al., 2007, Astrophys. J. Sup. S., 172, 615
Hinshaw G., et al., 2009, Astrophys. J. Sup. S., 180, 225
Hogg D. W., Blandford R. D., 1994, Month. Not. Roy. Astr. Soc., 268, 889
Jackson N., Xanthopoulos E., Browne I. W. A., 2000, Month. Not. Roy. Astr. Soc., 311, 389
Jiang G., Kochanek C. S., 2007, Astrophys. J., 671, 1568
Jørgensen I., Franx M., Kjaergaard P., 1996, Month. Not. Roy. Astr. Soc., 280, 167
Kauffmann G., White S. D. M., Guiderdoni B., 1993, Month. Not. Roy. Astr. Soc., 264, 201
Keeton C. R., et al., 2000, Astrophys. J., 542, 74
Krist J., 1993, in R. J. Hanisch, R. J. V. Brissenden, & J. Barnes ed., Astronomical Data Analysis Software and Systems II Vol. 52 of Astronomical Society of the Pacific Conference Series, Tiny Tim : an HST PSF Simulator. pp 536–+
Kroupa P., Tout C. A., Gilmore G., 1993, Month. Not. Roy. Astr. Soc., 262, 545
Larson R. B., 1974, Month. Not. Roy. Astr. Soc., 169, 229
Lehár J., et al., 2000, Astrophys. J., 536, 584
Leier D., 2009, Month. Not. Roy. Astr. Soc., 400, 875
Liesenborgs J., de Rijcke S., Dejonghe H., Bekaert P., 2008, Month. Not. Roy. Astr. Soc., 386, 307
Lintott C. J., Ferreras I., Lahav O., 2006, Astrophys. J., 648, 826
Lopez S., Wucknitz O., Wisotzki L., 1998, Astron. & Astrophys., 339, L13
Mandelbaum R., Seljak U., Kauffmann G., Hirata C. M., Brinkmann J., 2006, Month. Not. Roy. Astr. Soc., 368, 715
McKean J. P., Koopmans L. V. E., Flack C. E., Fassnacht C. D., Thompson D., Matthews K., Blandford R. D., Readhead A. C. S., Soifer B. T., 2007, Month. Not. Roy. Astr. Soc., 378, 109
Miller G. E., Scalo J. M., 1979, Astrophys. J. Sup. S., 41, 513
Momcheva I., Williams K., Keeton C., Zabludoff A., 2006, Astrophys. J., 641, 169
More A., McKean J. P., More S., Porcas R. W., Koopmans L. V. E., Garrett M. A., 2009, Month. Not. Roy. Astr. Soc., 394, 174
Morgan N. D., Chartas G., Malm M., Bautz M. W., Burud I., Hjorth J., Jones S. E., Schechter P. L., 2001, Astrophys. J., 555, 1
Moster B. P., Somerville R. S., Maulbetsch C., van den Bosch F. C., Macciò A. V., Naab T., Oser L., 2010, Astrophys. J., 710, 903
Muñoz J. A., et al., 2001, Astrophys. J., 546, 769
Peng C. Y., Ho L. C., Impey C. D., Rix H., 2002, Astron. J., 124, 266

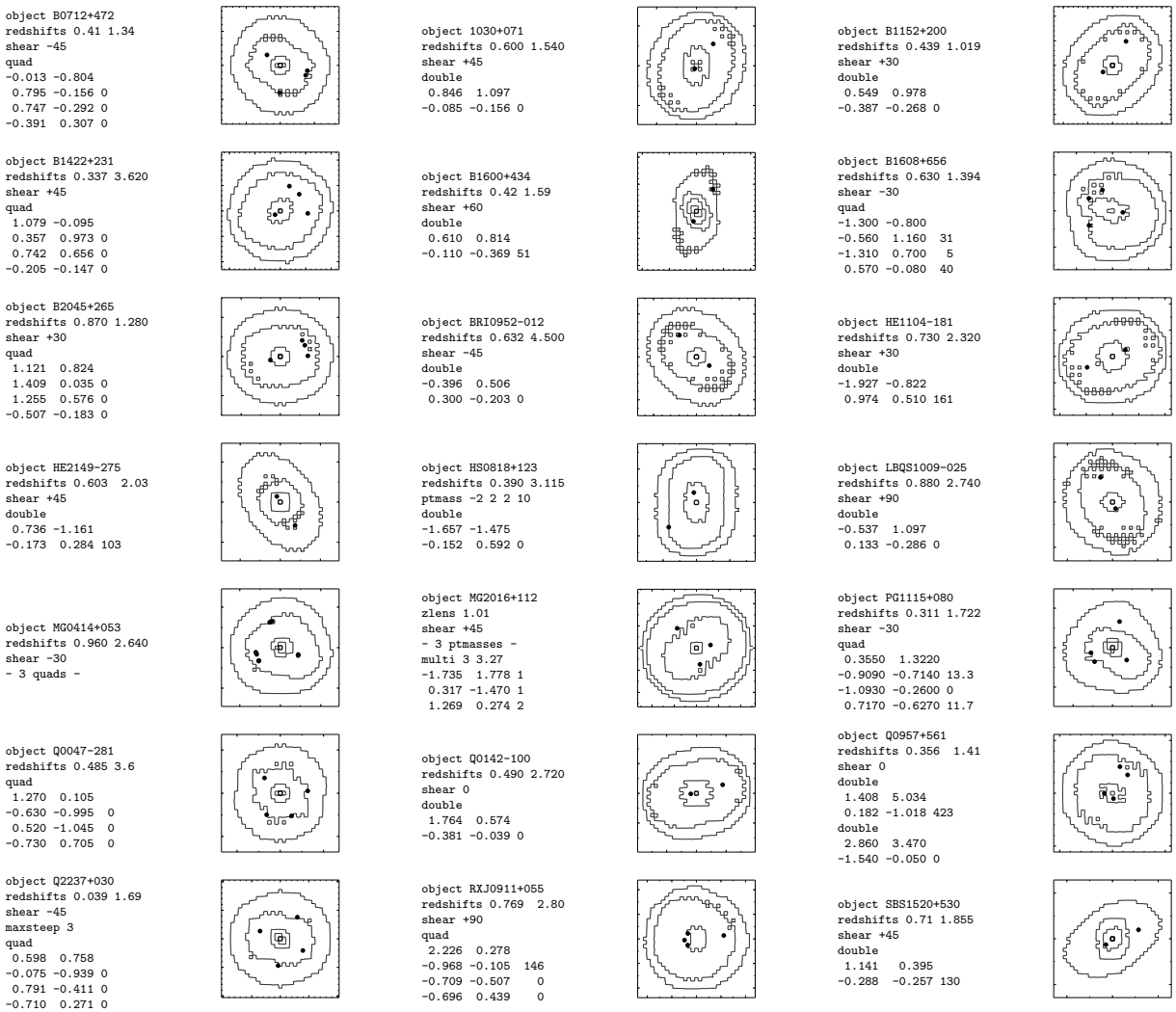

FIG. 15.— PIXELENS input data and projected mass distribution for the lens sample. The black dots mark the multiple images. All maps have a radius of 15 pixel. All mass maps have a radius of 2 $R_{\rm lens}$, which corresponds roughly to 2 $R_{\rm Ein}$. All lens properties as well as respective length specifications are in Table 1.

Peng C. Y., Impey C. D., Rix H., Kochanek C. S., Keeton C. R., Falco E. E., Lehár J., McLeod B. A., 2006, Astrophys. J., 649, 616

Popović L. Č., Moiseev A. V., Mediavilla E., Jovanović P., Ilić D., Kovačević J., Muñoz J. A., 2010, Astrophys. J. Let., 721, L139

Rogers B., Ferreras I., Peletier R., Silk J., 2010, Month. Not. Roy. Astr. Soc., 402, 447

Rusin D., Kochanek C. S., Keeton C. R., 2003, Astrophys. J., 595, 29

Saha P., 2000, Astron. J., 120, 1654

Saha P., Williams L. L. R., 2004, Astron. J., 127, 2604

Salpeter E. E., 1955, Astrophys. J., 121, 161

Scalo J. M., 1986, Fundamentals of Cosmic Physics, 11, 1

Schechter P. L., Moore C. B., 1993, Astron. J., 105, 1

Schlegel D. J., Finkbeiner D. P., Davis M., 1998, Astrophys. J., 500, 525

Shen S., Mo H. J., White S. D. M., Blanton M. R., Kauffmann G., Voges W., Brinkmann J., Csabai I., 2003, Month. Not. Roy. Astr. Soc., 343, 978

Sijacki D., Springel V., Di Matteo T., Hernquist L., 2007, Month. Not. Roy. Astr. Soc., 380, 877

Surdej J., et al., 1987, Nature, 329, 695

Sykes C. M., et al., 1998, Month. Not. Roy. Astr. Soc., 301, 310

Tabor G., Binney J., 1993, Month. Not. Roy. Astr. Soc., 263, 323

Toft S., Soucail G., Hjorth J., 2003, Month. Not. Roy. Astr. Soc., 344, 337

Tonry J. L., Kochanek C. S., 1999, Astron. J., 117, 2034

Tremonti C. A., et al., 2004, Astrophys. J., 613, 898

Treu T., Gavazzi R., Gorecki A., Marshall P. J., Koopmans L. V. E., Bolton A. S., Moustakas L. A., Burles S., 2009, Astrophys. J., 690, 670

Trott C. M., Treu T., Koopmans L. V. E., Webster R. L., 2010, Month. Not. Roy. Astr. Soc., 401, 1540

van Dokkum P. G., Franx M., Fabricant D., Illingworth G. D., Kelson D. D., 2000, Astrophys. J., 541, 95

Walsh D., Carswell R. F., Weymann R. J., 1979, Nature, 279, 381

Wisotzki L., Wucknitz O., Lopez S., Sorensen A. N., 1998, Astron. & Astrophys., 339, L73

Wong, K. C., Keeton, C. R., Williams, K. A., Momcheva, I. G., Zabludoff, A. I., 2011, Astrophys. J., 726, 84

Yamauchi C., et al., 2005, Astron. J., 130, 1545

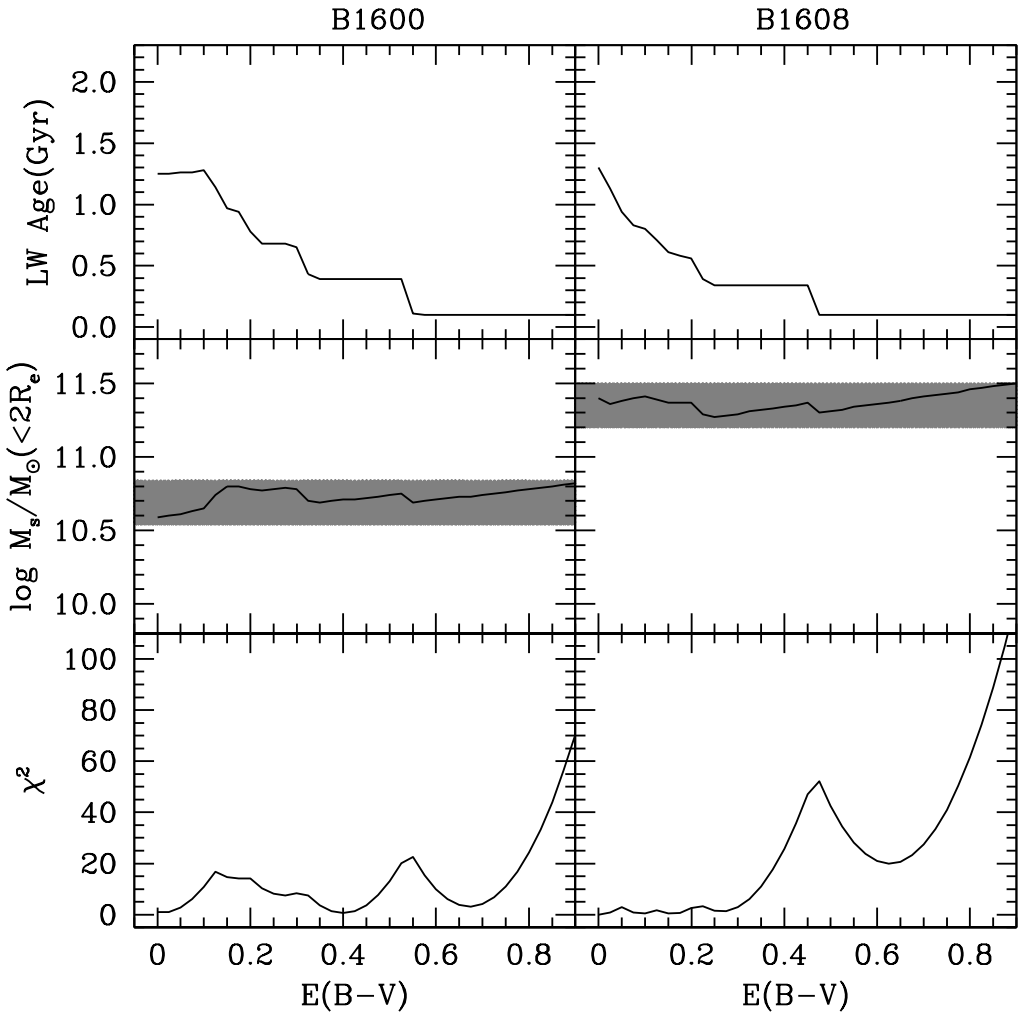

FIG. 16.— From top to bottom: Age, stellar mass and minimum χ^2 versus reddening for the lenses B1600 and B1608.